



Large-eddy simulations of conical hypersonic turbulent boundary layers over cooled walls via volumetric rescaling method

Takahiko Toki^{1,†}, Victor C.B. Sousa¹, Yongkai Chen¹,
Giannino Ponchio Camillo², Alexander Wagner² and Carlo Scalo^{1,3}

¹School of Mechanical Engineering, Purdue University, West Lafayette, IN 47907, USA

²German Aerospace Center (DLR), Institute of Aerodynamics and Flow Technology, 37073 Göttingen, Germany

³School of Aeronautics and Astronautics, Purdue University, West Lafayette, IN 47907, USA

(Received 15 July 2024; revised 12 December 2024; accepted 12 December 2024)

Large-eddy simulations (LES) of a hypersonic boundary layer on a 7° -half-angle cone are performed to investigate the effects of highly cooled walls (wall-to-recovery temperature ratio of $T_w/T_r \sim 0.1$) on fully developed turbulence and to validate a newly developed rescaling method based on volumetric flow extraction. Two Reynolds numbers are considered, $Re_m = 4.1 \times 10^6 \text{ m}^{-1}$ and $6.4 \times 10^6 \text{ m}^{-1}$, at free-stream Mach numbers of $M_\infty = 7.4$. A comparison with a reference laminar-to-turbulent simulation, capturing the full history of the transitional flow dynamics, reveals that the volumetric rescaling method can generate a synthetic turbulent inflow that preserves the structure of the fluctuations. Equilibrium conditions are recovered after approximately 40 inlet boundary layer thicknesses. Numerical trials show that a longer streamwise extent of the rescaling box increases numerical stability. Analyses of turbulent statistics and flow visualizations reveal strong pressure oscillations, up to 50% of local mean pressure near the wall, and two-dimensional longitudinal wave structures resembling second-mode waves, with wavelengths up to 50% of the boundary layer thickness, and convective Mach numbers of $M_c \simeq 4.5$. It is shown that their quasi-periodic recurrence in the flow is not an artefact of the rescaling method. Strong and localized temperature fluctuations and spikes in the wall-heat flux are associated with such waves. Very high values of temperature variance near the wall result in oscillations of the wall-heat flux exceeding its average. Instances of near-wall temperature falling below the imposed wall temperature of $T_w = 300 \text{ K}$ result in pockets of instantaneous heat flux oriented against the statistical mean direction.

Key words: hypersonic flow, compressible turbulence, turbulent boundary layers

† Email address for correspondence: ttoki@purdue.edu

© The Author(s), 2025. Published by Cambridge University Press. This is an Open Access article, distributed under the terms of the Creative Commons Attribution licence (<http://creativecommons.org/licenses/by/4.0>), which permits unrestricted re-use, distribution and reproduction, provided the original article is properly cited.

1. Introduction

1.1. Motivation

Turbulent boundary layers on hypersonic vehicles entail significant skin friction and, more importantly, heating loads. Accurate prediction of the state of the boundary layer on hypersonic vehicles is of paramount importance in reducing the redundancies in the thermal protection systems. Reynolds-averaged Navier–Stokes (RANS) simulations are generally adopted in engineering application designs because of their relatively low computational costs (Bertin & Cummings 2006), although they are known to grossly over or underpredict the skin friction and heat transfer in the high-speed regime (Wilcox 2006; Rumsey 2010; Aiken *et al.* 2022; Hendrickson *et al.* 2023; Parish *et al.* 2023). While several studies proposed compressibility corrections for improvements of RANS models and achieved significant improvements in the prediction (McDaniel *et al.* 2016; Nichols 2019; Danis & Durbin 2022; Hendrickson, Subbareddy & Candler 2022; Parish *et al.* 2023; Chen, Gan & Fu 2024; Xue, Feng & Zheng 2024), high-fidelity, or eddy-resolving, methods like large-eddy simulations (LES) or direct numerical simulations (DNS) are still needed to correctly predict the dynamics of turbulent fluctuations. The latter may reach surprising values in wall-bounded hypersonic flows, especially under high cooling ratios. Associated high-frequency mechanical vibrations are also a concern when wall-pressure fluctuations exceed critical levels, entailing significant dynamic loading for the vehicle aeroshell already experiencing a large thermal load. This manuscript investigates the fundamental structure of near-wall hypersonic turbulence under highly cooled conditions, with a newly developed LES methodology (Sousa & Scalo 2022*b*; Pati *et al.* 2024), comparing results against recent DNS investigations (Huang *et al.* 2020; Huang, Duan & Choudhari 2022; Roy, Kuchta & Duan 2024), while also attempting to inform typical closures of interest to the RANS community (Slotnick *et al.* 2014; Cary *et al.* 2021; Xue *et al.* 2024).

Numerous DNS and LES studies have been conducted to investigate the flow dynamics in hypersonic boundary layers, especially for flat plate geometries (Zhang, Duan & Choudhari 2018). The main findings from notable DNS studies are summarized in § 1.2. Mach numbers of these studies are up to 20 and a wall-to-recovery temperature ratio, T_w/T_r , ranges from 0.15 to 1.0. More recent DNS studies revealed unique small-scale unsteady phenomena when the wall is highly cooled (Chen & Scalo 2021*b*; Roy *et al.* 2024; Toki *et al.* 2024), inspiring a deeper dive into near-wall turbulent dynamic under strong heat-flux conditions, that is, with a lower wall-to-recovery temperature ratio T_w/T_r than past DNS and LES studies reviewed in § 1.2. The present study also investigates the performance of a newly developed rescaling strategy relying on volumetric flow extraction, as opposed to more common rescaling methods (reviewed in § 1.3) operating with two-dimensional cross-flow slices of the flow.

1.2. High-fidelity simulations of hypersonic boundary layers

Pioneering works of high-fidelity simulations of hypersonic boundary layers are attributed to Martin (2004, 2007), where a local initialization procedure to simulate temporal supersonic and hypersonic boundary layers with Mach numbers up to 8 was first introduced. Duan, Beekman & Martin (2010, 2011) and Duan & Martin (2011) extended such a dataset by exploring the effects of cold wall temperature, Mach number and high enthalpy. Mach numbers investigated were up to 12, with temperature ratios in the range $T_w/T_r = 0.18$ –1.0. It was revealed that turbulent flow structures and thermodynamic fluctuations are strongly affected by the wall temperature and the boundary-layer edge

Mach number. Unexpectedly, many of the scaling relations used to express adiabatic compressible boundary layers were found to hold for non-adiabatic cases. In particular, Kármán's constant in the Van Driest transformed velocity is insensitive to wall temperature and the semi-local scaling (Huang, Coleman & Bradshaw 1995) works well for the turbulent kinetic energy budget.

Lagha *et al.* (2011) explored a wider range of Mach numbers, from 2.5 to 20, and pointed out significant changes in the dilatation field, which can be scaled with a density-based normalization. Huang *et al.* (2022) investigated the spatial evolution over a long streamwise domain, showing that low-Reynolds-number scaling relations still hold up to a frictional Reynolds number of $Re_\tau \approx 1200$. Xu *et al.* (2021*a,b*) and Xu, Wang & Chen (2022) conducted DNS of hypersonic boundary layers focusing on the effects of wall temperature, and investigated turbulent correlations, kinetic energy, skin friction and wall-heat transfer. Recently, Di Renzo & Urzay (2021) simulated a hypersonic transitional boundary layer including aerothermochemistry effects using DNS, and provided several statistics regarding interactions with turbulent fluctuations. Passiatore *et al.* (2021, 2022) also conducted DNS under similar conditions, extending their scope to thermochemical non-equilibrium.

While numerous high-fidelity studies at fully turbulent conditions have been conducted for flat plate boundary layers, fewer studies of the same type appear for conical geometries, which are more often investigated at transitional conditions. Li, Fu & Ma (2008) conducted DNS of transitional flow around a blunt cone at Mach 6, and reported that second-mode waves are the dominant transition mechanism. Sivasubramanian & Fasel (2015) performed DNS over a sharp cone at Mach 6 (Casper *et al.* 2009; Alba *et al.* 2010) focusing on the nonlinear interactions during the turbulent breakdown process. Huang *et al.* (2024) carried out DNS for the same geometry at Mach 8 based on the experiments in the Sandia Hypersonic Wind tunnel (Casper *et al.* 2013, 2016). They compared the power spectral density of wall-pressure fluctuations between the DNS and the experiments. Sousa *et al.* (2024) simulated the full path to turbulent breakdown using the same LES approach as the present study based on experiments conducted by Wagner *et al.* (2013) in the DLR High Enthalpy Shock Tunnel Göttingen, HEG (Deutsches Zentrum für Luft - und Raumfahrt -DLR 2018). They imposed pseudo-random pressure perturbations in a volume located upstream over the surface of the cone to mimic natural transition conditions. To our knowledge, this is the first dynamic LES of a transitional hypersonic boundary layer.

Fully turbulent high-fidelity calculations over conical geometries are still limited, which motivates the computational set-up chosen by this study. In addition, recent DNS studies on canonical doubly periodic flows revealed that highly cooled conditions yield unique flow structures near the wall, which required verification in the case of spatially developing flows. For example, Chen & Scalò (2021*b*) simulated hypersonic channel flows up to bulk Mach numbers of $M_b = 6.0$ and revealed the presence of streamwise-travelling trapped pressure waves similar to second-mode instabilities. Toki *et al.* (2024) simulated hypersonic Couette flow with $T_w/T_r \simeq 0.11$, and found that strong sub-filter-scale counter-gradient momentum transport occurs in the buffer region due to the strong thermal and density gradient. The present investigation looks at sharp cone geometries at $T_w/T_r \simeq 0.1$, revealing similar flow structures due to the highly cooled conditions. To the best of the authors' knowledge, the temperature ratio investigated herein is the lowest found in the literature and, while not relevant for flight conditions, it is a natural outcome of short-duration, high-enthalpy ground testing.

1.3. Rescaling methods

The present investigation relies on a new type of volumetric rescaling strategy, which was inspired by the adopted quasi-spectral numerical discretization method. Several kinds of rescaling methods have been proposed in the past, and they are briefly summarized here.

Lund, Wu & Squires (1998) proposed the first rescaling method to produce realistic inflow conditions for incompressible spatially evolving boundary layers. They extracted the velocity field from a plane near the domain exit, rescaled it based on self-similar scaling laws and reintroduced it as the inflow boundary condition. Within the context of the same method, Simens *et al.* (2009) established that the extraction plane should be at least 20–30 boundary layer thicknesses away from the inflow to achieve sufficient decorrelation. Araya *et al.* (2011) proposed a dynamic multi-scale approach, relying on the adoption of a test plane located between the inlet and extraction planes to inform the choice of the assumed convective scaling laws.

Urbin & Knight (2001) and Stolz & Adams (2003) extended the rescaling method to compressible flows. Urbin & Knight (2001) adopted the Van Driest–Fernholz and Finley transformation, adopting a mixed rescaling for the temperature field, involving wall units and outer-layer scaling. Stolz & Adams (2003) used the Van Driest transformation for the velocity scaling, and applied inner and outer scalings for temperature and density. Xu & Martin (2004) also developed a rescaling method for compressible boundary layers, based on Morkovin’s hypothesis (Bradshaw 1977) and a generalized temperature–velocity relationship. Sagaut *et al.* (2004) evaluated several rescaling methods for compressible boundary layers, and reported that, if not controlled, the boundary layer thickness at the inflow can drift from the target value over long integration times. To avoid this, they proposed freezing the mean inflow velocity profile based on data obtained by other methodologies such as RANS simulations or experiments. Lagha *et al.* (2011) adopted an approximation for the mean temperature using the Crocco–Busemann relation and the mean velocity profile with Reichardt’s inner-layer solution and Finley’s wake function. Morgan *et al.* (2011) reported that rescaling strategies can contaminate the solution with spurious spatio-temporal correlations introduced by convective time lapse between the inflow and the extraction plane. They demonstrated that these correlations can be removed by applying a non-constant reflection or translation operation to the recycled plane. Duan, Choudhari & Wu (2014) modified the rescaling method of Xu & Martin (2004) by adding dynamics translation operations following Morgan *et al.* (2011), and applied a filter to the free stream to remove artificial inlet acoustics that may be introduced due to the coupling between the recycling and inflow plane. Finally, Kianvashrad & Knight (2021) used the mean total enthalpy to compute the mean temperature at the inflow boundary and demonstrated that their method shows improvements in terms of the Reynolds analogy and turbulent Prandtl number.

These rescaling strategies have been successfully employed in many high-fidelity simulations of compressible boundary layers, whereas their applications have been mostly limited to flat plate geometries because of the better-established self-similar scaling laws. Therefore, alternative approaches like the digital-filtering method (Dhamankara, Blaisdella & Lyrintzis 2016) have been used for conical geometries (Huang *et al.* 2024). Ceci *et al.* (2022) compared the digital-filtering and rescaling methods in supersonic and hypersonic boundary layers, and summarized the advantages and disadvantages of both methods. However, the digital-filtering method requires a longer recovery length for flat plate boundary-layer calculations, as compared with rescaling strategies (Huang *et al.* 2022). Since shorter recovery lengths lead to more efficient usage of computational domains, the rescaling method is still an attractive approach, which we extend to a conical geometry. This study develops a new rescaling strategy: the volumetric rescaling method,

and applies it to conical hypersonic boundary layers. The results from the proposed rescaling method are compared against previously published calculations by the same authors (Sousa *et al.* 2024) that capture the full laminar-to-turbulent transition path. These two computational set-ups are not expected to match due to the well-known long streamwise coherence of transitional structures, subject to very different dynamics than what is entailed by the pseudo-periodic rescaling of the present calculations. In spite of such fundamental differences, there is good agreement between the two approaches on quantities like the average wall-heat flux.

1.4. Paper outline

The remaining paper is organized as follows. The computational conditions and numerical set-ups are summarized in §2. The current rescaling technique is described in §2.3. The grid sensitivity analyses are provided in §3. The performance of the proposed rescaling method is examined in §4. Results are compared with reference data from a laminar-to-turbulent transition simulation under the same flow condition in §4.1. The recovery length is discussed by analysing the turbulent statistics and temperature–velocity relationship in §§4.2 and 4.3. A sensitivity analysis of the rescaling box size is carried out in §4.4. Near-wall flow dynamics in conical hypersonic boundary layers is explored in §5. The temperature–velocity relationship for mean profiles is compared against several correlations such as the Crocco–Busemann relation in §5.1. Turbulent statistics and the strong Reynolds analogy are investigated in §5.2. Flow fields are visualized in §5.3 with particular attention to the relationship between flow structures and the turbulent statistics in §5.2. The findings from this study are summarized in §6.

2. Problem formulation

2.1. Flow conditions

The numerical study performed in this work is based on experiments conducted in the DLR High Enthalpy Shock Tunnel Göttingen, HEG (Wagner 2014; Deutsches Zentrum für Luft - und Raumfahrt -DLR 2018; Wagner *et al.* 2019). The present configuration is a hypersonic boundary layer over a 7-degree half-angle cone, and test conditions of $Re_m = 4.1 \times 10^6 \text{ m}^{-1}$ and $Re_m = 6.4 \times 10^6 \text{ m}^{-1}$ are chosen. In table 1, $Re_m \equiv \rho_\infty u_\infty / \mu_\infty$ is the Reynolds number per metre, p is pressure, T is temperature, ρ is density, u is velocity and M is Mach number. The subscript ∞ indicates free-stream conditions. The wall temperature T_w is 300 K for all cases, and it is consistent with the experiment because of the short duration of the test run. The T_w/T_r is wall-to-recovery temperature ratio, where T_r is defined as

$$T_r \equiv T_\infty \left(1 + r_{turb} \frac{\gamma - 1}{2} M_\infty^2 \right), \quad (2.1)$$

where γ is the specific heat ratio ($\gamma = 1.4$). The parameter r_{turb} is a recovery factor for turbulent boundary layers and it can be approximated as $r_{turb} \approx Pr^{1/3}$ (Dorrance 1962; White 2006), where Pr is the Prandtl number ($Pr = 0.707$). Since the free-stream temperature is high, the wall-to-recovery temperature ratio decreases to approximately 0.1. Figure 1 provides a sketch of the present configuration. In the experiment, a conical shock is attached to the tip of the cone, and a boundary layer is formed on the cone surface only under the shock. The laminar boundary layer starts from the tip and the transition to turbulence happens further downstream on the surface. In this study, the turbulent region

Case	Re_m (m^{-1})	p_∞ (Pa)	T_∞ (K)	ρ_∞ ($kg\ m^{-3}$)	u_∞ ($m\ s^{-1}$)	M_∞	T_w (K)	T_w/T_r	Inflow method
M7.4-R4.1	4.1×10^6	2129	268	0.0276	2422	7.4	300	0.104	rescaling
M7.4-R6.4	6.4×10^6	3083	248	0.0432	2350	7.4	300	0.112	rescaling
M7.4-LT4.1	4.1×10^6	2129	268	0.0276	2422	7.4	300	0.104	transitional

Table 1. List of computational cases and conditions. All symbols are defined in the text.

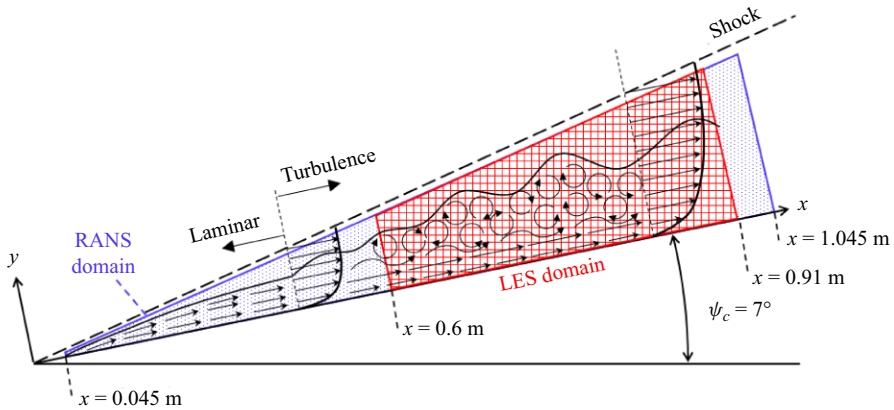


Figure 1. Sketch of the present conical hypersonic boundary-layer configuration.

under the shock is simulated with the two Reynolds numbers (M7.4-R4.1 and M7.4-R6.4) using our proposed volumetric rescaling method described in § 2.3. A simulation including the laminar-to-turbulent transition with $Re_m = 4.1 \times 10^6\ m^{-1}$ (M7.4-LT4.1) is used as reference data. This case has been simulated in previous work by the same authors (Sousa *et al.* 2024). In the present simulation, the computational domain is wider in the azimuthal direction, and the mesh is finer in the wall-normal direction. These computational cases are summarized in table 1.

2.2. Flow set-up

A precursor axisymmetric RANS simulation is carried out for the present rescaling simulations. The inlet of the RANS computational domain is located in the $x = 0.045\ m$ plane, where x is the distance from the cone tip along the wall surface. The domain length in streamwise direction L_x extends 1 m. The domain height in the wall-normal direction L_y is 0.0022 m at the inlet and 0.05 m at the outlet. These lengths are decided so that the upper domain boundary stays under the shock. The azimuthal extension θ is 1.5° . The flow properties at the upper boundary are analytically derived by the Taylor–Maccoll inviscid solution (Taylor & Maccoll 1933), and those at the inlet and outlet are given by combining the Taylor–Maccoll inviscid solution with a viscous solution for the cone boundary layer (Lees 1956). Sponge layers are used at the inlet, outlet and upper boundaries. All flow quantities are gradually relaxed to the Taylor–Maccoll inviscid solution in the upper boundary or to a blending of Blasius and Taylor–Maccoll in the inlet or outlet. The length of the sponge layers at the inlet and outlet is 3 % of the total computational domain extent in the streamwise direction. That at the upper boundary is 5 % of the wall-normal extent. At the wall, a no-slip isothermal boundary condition is imposed with the wall temperature of

300 K. Periodic boundary conditions are imposed in the azimuthal direction. The number of grid points is $N_x \times N_y \times N_\theta = 5120 \times 256 \times 6$. The Spalart–Allmaras (SA) model (Spalart & Allmaras 1992) is used as a RANS model. To simulate a turbulent transition in a boundary layer, the SA model uses a trip source term for the eddy viscosity. The trip location is decided based on the experiment by Wagner *et al.* (2019) and it is at $x = 0.3$ m.

Only a part of the RANS computational domain is simulated in the present rescaled LES. Figure 2 shows the domain length and relative positions of the rescaling and recycling boxes. The inlet of the rescaled LES is located at $x = 0.6$ m, and its domain length in the streamwise direction L_x is 0.31 m. The azimuthal angle θ is extended to 18° , which is the same as the authors’ past work (Camillo *et al.* 2023). Moreover, the two-point correlations (shown in figure 27 in § 5.3) confirm the adequacy of this choice. The inlet profiles of mean quantities are given by the RANS results at $x = 0.6$ m. The inflow turbulence is established by the volumetric rescaling method and its details are provided in § 2.3. Sponge layers are imposed at the outlet and the upper boundaries, and all flow quantities are gradually relaxed to be the solution obtained by the precursor RANS. The ratios of the sponge layers are the same as the precursor RANS, however, their streamwise lengths are shorter because of the different L_x . Effects of the sponge layers on turbulent statistics are examined in Appendix B. The inlet of the laminar-to-turbulent transition case is located at $x = 0.1$ m, and its domain length in the streamwise direction L_x is 0.9 m. The flow properties at the inlet are decided by the Taylor–Maccoll inviscid solution (Taylor & Maccoll 1933) and a viscous solution for the cone boundary layer (Lees 1956) in the same manner as the RANS. To induce laminar–turbulent transition, pseudorandom pressure perturbations are added in the laminar region. The perturbations were described in detail elsewhere (Sousa *et al.* 2024).

The number of grid points is $N_x \times N_y \times N_\theta = 1600 \times 256 \times 160$ for the rescaling cases (M7.4-R4.1 and M7.4-R6.4). A coarse mesh of $N_x \times N_y \times N_\theta = 960 \times 128 \times 84$ is also used in M7.4-R4.1 only to discuss the effects of the rescaling box size in § 4.4. The grid for the laminar–turbulent transition case (M7.4-LT4.1) is $N_x \times N_y \times N_\theta = 3072 \times 192 \times 160$, which is coarser than the one for M7.4-R4.1 because of the requirements for a larger computational domain. The effects of the different grid resolutions are examined in § 3. The grid spacing is uniform in the streamwise and azimuthal directions. The grid spacing in the wall-normal direction is stretched and clustered at the wall. The grid resolutions at $x = 0.85$ m are shown in table 2. They are evaluated as $\Delta x_i^+ \equiv \rho_w \Delta x_i u_\tau / \mu_w$, where $u_\tau \equiv \sqrt{\tau_w / \rho_w}$ is the friction velocity, τ_w is the wall-shear stress and Δx_i is the grid spacing in the x_i direction; Δx^+ and Δz^+ are the grid resolutions in the streamwise and azimuthal directions, respectively. In this paper, z is the coordinate in the azimuthal direction along the curved surface at each x location. The wall-normal grid spacing Δy_1^+ corresponds to that at the bottom of the domain. The parameter $Re_\Theta \equiv u_e \Theta \rho_e / \mu_e$ is the Reynolds number based on the momentum thickness Θ . The parameter $Re_\tau \equiv u_\tau \delta \rho_w / \mu_w$ is the friction Reynolds number. The parameter $Re_\tau^* \equiv u_{\tau,e}^* \delta \rho_e / \mu_e$ is a semi-local friction Reynolds number, which accounts for variable density effects (Huang *et al.* 1995). The parameters ρ_e and μ_e are the density and viscosity at the edge of the boundary layer. The parameter $u_{\tau,e}^* \equiv \sqrt{\tau_w / \rho_e}$ is a semi-local friction velocity. The grid resolutions in the star unit are obtained by $\Delta x_i^* \equiv \Delta x_i^+ Re_\tau^* / Re_\tau$.

The rescaling simulations undergo a long temporal transient until the flow field reaches a steady state, as shown in the authors’ past work (Camillo *et al.* 2023). In the present study, the wall-shear stress and heat flux are monitored and, after they reach the steady state, statistical datasets for the rescaling cases are obtained by spatial averaging in the azimuthal direction and time averaging during a period of approximately $100\delta / u_\infty$ based

are given by RANS calculations, and (ii) fluctuations are extracted from a certain volume and not a plane.

As summarized in § 1.3, general rescaling methods decide mean profiles based on scaling laws such as the Van Driest transformation. However, most scaling laws do not account for the conical expansion of flow in the downstream direction. Therefore, a precursor axisymmetric RANS simulation is carried out in this study and used as the mean inflow instead of scaling laws. Such usage of RANS results was proposed to avoid the drift of mean profiles at the inflow by Sagaut *et al.* (2004).

General rescaling methods extract turbulent fluctuations from a plane at a certain streamwise coordinate, which are then rescaled and added to a mean profile at the inlet boundary. Since the imposed variables do not perfectly satisfy the governing equations at the inlet, adjustments accompanied by non-physical pressure oscillations occur around the rescaling plane. This is especially true with low-dissipation numerics such as the high-order compact finite differencing schemes (Lele 1992) used in the present calculation. Spectral-like schemes will not accommodate the non-physical steep flow gradients imposed by a classic planar rescaling strategy, especially at hypersonic conditions.

To allow for proper numerical relaxation of the rescaled fluctuations in a spectral solver, the present study extracts the three-dimensional fluctuating field from a recycling box with a finite extent in the streamwise direction. Such fluctuations are then applied to a rescaling box near the inlet. Numerical trials have shown that excessively small rescaling volumes lead to numerical instabilities, as shown in § 4.4. Due to the spectral nature of the numerics, a sufficient number of streamwise points are needed within the rescaling box to guarantee the robustness of the numerical reconstruction and smoothness of the flow field downstream of it.

The present rescaling procedure is as follows. The formulations for rescaled fluctuations are the same as Stolz & Adams (2003) method. The velocity fluctuations u'_i in the recycling box are computed as

$$u'_i = u_i - \langle u_i \rangle. \quad (2.2)$$

The notations $(\cdot)'$ and $(\cdot)''$ indicate fluctuations in the average and the Favre average in this paper. The bracket operators $\langle \cdot \rangle$ and $\{ \cdot \}$ indicate averaging and Favre averaging in time and the azimuthal direction, respectively. The velocity fluctuations imposed in the rescaling box are computed from the extracted fluctuations in the recycling box by using the following scaling:

$$\frac{u'_{i,in}}{u_\tau} = G_{in,u'_i}(y^+) \quad \text{and} \quad \frac{u'_{i,out}}{u_\tau} = G_{out,u'_i}(\eta). \quad (2.3a,b)$$

The subscripts *in* and *out* indicate inner- and outer-layer scalings, respectively. Here, η is the outer-layer coordinate y/δ and the functions G_{in,u'_i} and G_{out,u'_i} are assumed not to depend on the streamwise coordinate x . These scaling functions are unknown during the simulation, however, the imposed fluctuations can be obtained by interpolating the fluctuations extracted from the recycling box based on the y^+ and η coordinates. The density and temperature fluctuations are computed similarly, but they are scaled by their values at the edge of the boundary layer. The scaling laws are expressed as

$$\frac{T'_{in}}{T_e} = G_{in,T'}(y^+), \quad \frac{T'_{out}}{T_e} = G_{out,T'}(\eta), \quad (2.4a,b)$$

$$\frac{\rho'_{in}}{\rho_e} = G_{in,\rho'}(y^+), \quad \frac{\rho'_{out}}{\rho_e} = G_{out,\rho'}(\eta). \quad (2.5a,b)$$

The fluctuations for the inner and outer layers are blended by the weighting function proposed by Lund *et al.* (1998) as

$$W(\eta) = \frac{1}{2} \left[1 + \left(\tanh \left(\frac{\alpha(\eta - b)}{(1 - 2b)\eta + b} \right) / \tanh(\alpha) \right) \right], \quad (2.6)$$

with $\alpha = 4$ and $b = 0.2$. According to these scaling laws, the imposed flow field in the rescaling box is computed as

$$u'_i = (1 - W(\eta))u'_{i,in} + W(\eta)u'_{i,out}, \quad (2.7)$$

$$T' = (1 - W(\eta))T'_{in} + W(\eta)T'_{out}, \quad (2.8)$$

$$\rho' = (1 - W(\eta))\rho'_{in} + W(\eta)\rho'_{out}. \quad (2.9)$$

In Stolz & Adams (2003) method, the fluctuations are computed for the inflow plane. In the volumetric rescaling method, turbulent fluctuations for $0.830 \text{ m} \leq x \leq 0.849 \text{ m}$ (recycling box) are extracted and the fluctuations are scaled and imposed upon the RANS precursor flow for $0.600 \text{ m} \leq x \leq 0.619 \text{ m}$ (rescaling box). The recycling and rescaling boxes have the same number of grid points (e.g. $N_x \times N_y \times N_\theta = 100 \times 256 \times 160$ for the fine mesh). At each station x , i.e. for each (y, θ) plane, the rescaled fluctuations are interpolated only in the y direction based on the aforementioned scaling laws. In the present rescaled LES, the imposed fluctuations are separately computed by (2.7)–(2.9) at each x grid point and imposed onto the mean profiles obtained by the precursor RANS. The recycling and rescaling boxes have the same domain lengths in the x -direction, while those in the θ -direction are different because the computational domain expands in the direction of going downstream. Therefore, the mapping of the imposed fluctuations is linearly shrunken to match the rescaling box. To impose fluctuations only in a boundary layer, they are attenuated over $y = 0.005 \text{ m}$ by a tangent hyperbolic function. The distance between the centres of the recycling and rescaling boxes is 0.23 m . This length is equivalent to $53\delta_i$ in M7.4-R4.1 and $57\delta_i$ in M7.4-R6.4, where δ_i is the boundary-layer thickness based on 99% of the free-stream velocity at the inlet ($x = 0.6 \text{ m}$), and it is comparable to other rescaling studies of hypersonic boundary layers (Duan, Choudhari & Zhang 2016; Huang *et al.* 2022). The inlet boundary-layer thickness is $\delta_i = 0.0043 \text{ m}$ for M7.4-R4.1 and 0.0040 m for M7.4-R6.4. In addition, the autocorrelation function in the streamwise direction is investigated in Appendix A, demonstrating that a statistical decorrelation is achieved after approximately 50 mm from the centre of the rescaling box.

Of note, LES results obtained by the present rescaling strategy were compared with experiments conducted in the DLR HEG wind tunnel. The results are discussed with special attention given to the comparison between experimental and computational focused laser differential interferometry signals in Camillo *et al.* (2023).

2.4. Governing equations

The simulations are performed by solving the spatial filtered compressible Navier–Stokes equations in curvilinear coordinates generalized by Jordan (1999) and Nagarajan, Lele & Ferziger (2007). Here, we consider a structured grid in the physical space y to be

transformed to computational space \mathbf{x} in the present configuration:

$$x^j = x^i(y_1, y_2, y_3), \quad (2.10)$$

$$y_i = y_i(x^1, x^2, x^3), \quad (2.11)$$

where x^i and y_i are the i th coordinates of each respective system of reference. The governing equations are given as

$$\frac{\partial \overline{J\rho}}{\partial t} + \frac{\partial}{\partial x^j}(\overline{J\rho}\tilde{v}^j) = 0, \quad (2.12)$$

$$\frac{\partial \overline{J\rho}\tilde{v}^i}{\partial t} + \frac{\partial}{\partial x^j}(\overline{J\rho}\tilde{v}^i\tilde{v}^j + \overline{Jp}g^{ij} - J\tilde{\sigma}^{ij} + \overline{J\rho}\tau^{ij}) = -\Gamma_{qj}^i(\overline{J\rho}\tilde{v}^q\tilde{v}^j + \overline{Jp}g^{qj} - J\tilde{\sigma}^{qj} + \overline{J\rho}\tau^{qj}), \quad (2.13)$$

$$\frac{\partial \overline{JE}}{\partial t} + \frac{\partial}{\partial x^j}(\overline{J(E+p)}\tilde{v}^j + J\tilde{Q}^j) = \frac{\partial}{\partial x^k}(J\tilde{\sigma}^{kj}g_{ik}\tilde{v}^k) - \frac{\partial \overline{J\rho}C_p q^j}{\partial x^j}, \quad (2.14)$$

where J is the Jacobian of the transformation, which is the determinant of the Jacobi matrix ($J_{ij} = \partial y_i / \partial x^j$), t denotes time, E is total energy and C_p is the specific heat at constant pressure. The parameters τ^{ij} and q^j are sub-filter-scale (SFS) stress tensor and SFS temperature flux, and they are written as

$$\tau^{ij} = \widetilde{v^i v^j} - \tilde{v}^i \tilde{v}^j, \quad (2.15)$$

$$q^j = \widetilde{T v^j} - \tilde{T} \tilde{v}^j. \quad (2.16)$$

These SFS terms are modelled by the QSV method (Sousa & Scalò 2022b), which is capable of unifying shock capturing and SFS modelling under a LES mathematical framework based on the concept that both hydrodynamic turbulence and shock formation are characterized by the energy cascade from large to small scales due to nonlinear interactions (Frisch 1995; Gupta & Scalò 2018), and they should be treated in a similar fashion. The QSV approach was also developed to be applicable to unstructured grids, via a Legendre spectral viscosity (LSV) method (Sousa & Scalò 2022a). In the present study, the SFS kinetic energy advection $\lambda_j = \widetilde{v^k v^k v^j} - \tilde{v}^k \tilde{v}^k \tilde{v}^j$, and the SFS turbulent heat dissipation $\epsilon = \partial(\overline{\sigma^{ij} v^j}) / \partial x^j - \partial(\tilde{\sigma}^{ij} \tilde{v}^j) / \partial x^j$ are neglected for consistency with the QSV approach published in Sousa & Scalò (2022b) and used in Sousa *et al.* (2024). A closure for these terms has been proposed in a later publication by the same authors Sousa & Scalò (2022a) as part of a new SFS model called LSV applicable to block-spectral schemes for unstructured solvers.

The transformation between u_i and v^j is given by

$$v^j = u_i \frac{\partial x^j}{\partial y_i}. \quad (2.17)$$

The overline ($\overline{(\cdot)}$) and tilde ($\tilde{(\cdot)}$) are used for spatial filtering and density-weighted spatial filtering:

$$\bar{\phi}(x) = \int \phi(x - \xi) G(\xi, x) d\xi, \quad (2.18)$$

$$\tilde{\phi} = \frac{\overline{\rho\phi}}{\bar{\phi}}, \quad (2.19)$$

where $G(\xi, x)$ is the filtering kernel, which depends on filtering types. In (2.12)–(2.14), g_{ij} and g^{ij} are the covariant and contravariant metric tensors, respectively, and Γ_{qj}^i is the Christoffel symbol of the second kind. They are defined as

$$g_{ij} = \frac{\partial y_i \partial y_j}{\partial x^k \partial x^k}, \tag{2.20}$$

$$g^{ij} = \frac{\partial x^k \partial x^k}{\partial y_i \partial y_j}, \tag{2.21}$$

$$\Gamma_{qj}^i = \frac{\partial x^i}{\partial y_l} \frac{\partial^2 y_l}{\partial x^q \partial x^j}. \tag{2.22}$$

In the curvilinear frame of reference the total energy, the viscous stress tensor and the heat flux vector are described by slightly modified relations described below:

$$\frac{\bar{J}p}{\gamma - 1} = \bar{J}E - \frac{1}{2}\bar{J}\rho g_{ij} \tilde{v}^i \tilde{v}^j - \frac{1}{2}\bar{J}\rho g_{ij} \tau^{ij}, \tag{2.23}$$

$$\tilde{\sigma}^{ij} = \mu(\tilde{T}) \left(g^{ik} \frac{\partial \tilde{v}^i}{\partial x^k} + g^{ik} \frac{\partial \tilde{v}^j}{\partial x^k} - \frac{2}{3} g^{ij} \frac{\partial \tilde{v}^k}{\partial x^k} \right), \tag{2.24}$$

$$\tilde{Q}^j = -\frac{C_p \mu(\tilde{T})}{Pr} g^{ij} \frac{\partial \tilde{T}}{\partial x^i}, \tag{2.25}$$

where μ is the transport coefficient of viscosity. Sub-filter contributions resulting from nonlinearities involving the temperature dependency of viscosity are neglected for consistency with Sousa *et al.* (2024).

2.5. Numerical methods

In the QSV-LES technique, the governing equations combined with the ideal gas law $p = \rho R_{gas} T$ (R_{gas} is the gas constant) are solved via the sixth-order compact finite difference code CFDSU originally developed by Nagarajan, Lele & Ferziger (2003) and now under continued development at Purdue. The code CFDSU has been successfully applied to several wall-bounded hypersonic flows (Sousa *et al.* 2019; Chen & Scalo 2021a,b; Sousa *et al.* 2023; Toki *et al.* 2024). The solver adopts a staggered finite difference scheme. Thermodynamic properties such as density, pressure and temperature are stored at cell centres, while velocity components and their associated momentum are stored at cell faces. Since the sixth-order compact scheme is not applicable at boundaries, the order is reduced to the fourth one at two points from each boundary. The time integration is carried out by a four-stage third-order strong stability preserving Runge–Kutta scheme (Gottlieb 2005). To ensure time stability, the conservative variables are filtered using a sixth-order compact filter described by Lele (1992). Its filter coefficient is 0.495. The molecular transport coefficients of viscosity μ and thermal conductivity k are computed by Sutherland’s law.

3. Grid sensitivity analyses

The dynamic LES approach adopted for this study yields (by design) grid-dependent results. A grid sensitivity analysis is therefore warranted to assess the robustness of first- and second-order statistics to the grid size.

We simulated all cases with the three different grid resolutions, as shown in table 2. Figure 3 shows wall-heat flux profiles with data of the precursor RANS and the experiment

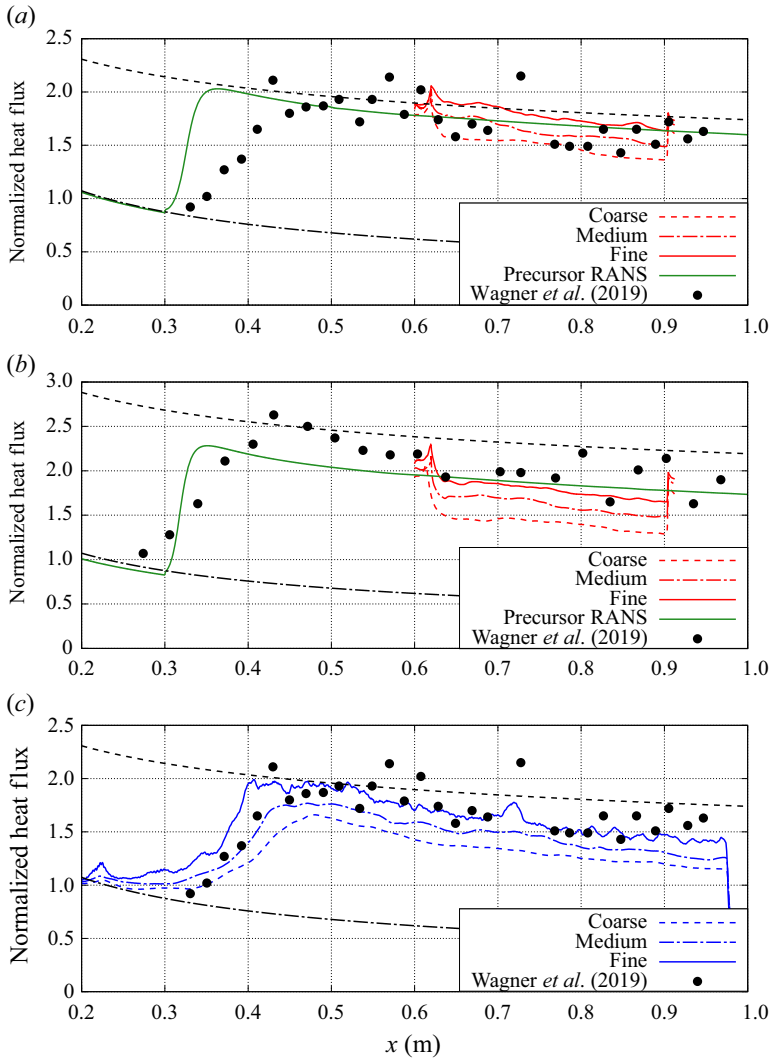


Figure 3. Grid sensitivity study for wall-heat flux in (a) M7.4-R4.1, (b) M7.4-R6.4 and (c) M7.4-LT4.1. The precursor RANS data are included for the rescaling cases. The experiments by Wagner *et al.* (2019) are also included for all panels. Correlations for the laminar cone boundary layers (Lees 1956) and turbulent ones (White 2006) are given by dash-dotted and dashed lines, respectively.

by Wagner *et al.* (2019). Correlations for the laminar cone boundary layers (Lees 1956) and turbulent ones (White 2006) are given by dash-dotted and dashed lines, respectively. The profiles are non-dimensionalized by the laminar correlation value at $x = 0.23$ m. The wall-heat flux approaches the experiment data and the semi-empirical correlation for turbulent heat flux as the grid is refined in all cases. In particular, the heat flux predictions in M7.4-R4.1 agree well with the experiment and the correlation. On the other hand, the data in M7.4-LT4.1 and M7.4-R6.4 slightly underestimate heat flux because of the relatively coarser resolution due to the absolute grid size spacing and higher Reynolds number, respectively.

Figure 4 shows wall transformed van Driest (1951) velocity profiles for each grid at $x = 0.85$ m. To account for wall-normal property variations, several velocity scaling laws

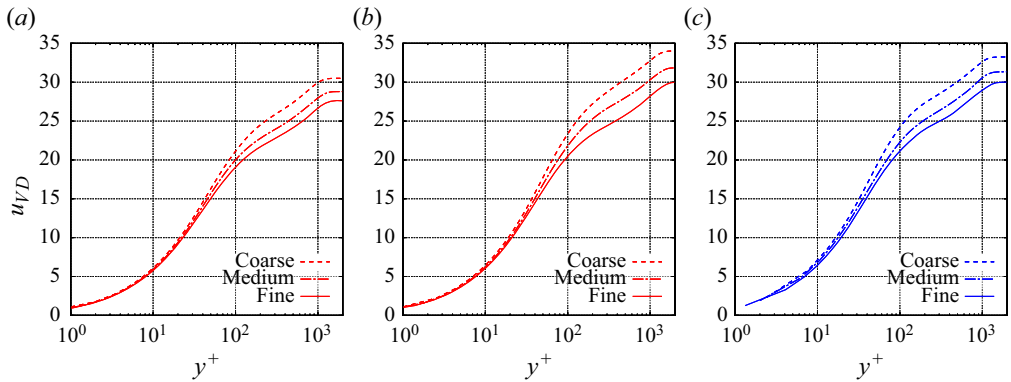


Figure 4. Grid sensitivity study for transformed velocity profiles via Van Driest transformation (van Driest 1951) at $x = 0.85$ m in (a) M7.4-R4.1, (b) M7.4-R6.4 and (c) M7.4-LT4.1.

are available in the literature (Zhang *et al.* 2012; Trettel & Larsson 2016; Volpiani *et al.* 2020; Griffin, Fu & Moin 2021; Bai, Griffin & Fu 2022; Hasan *et al.* 2023). For simplicity, van Driest (1951) transformation is adopted here, which is defined as

$$u_{VD} = \int_0^{u^+} \left(\frac{\langle \rho \rangle}{\langle \rho_w \rangle} \right)^{1/2} du^+. \quad (3.1)$$

The transformed velocity profiles show sensible behaviour with respect to grid refinements, with the intercept lowering as a broader spectrum of turbulent wall-shear stress is captured.

To further investigate grid sensitivity, figures 5 and 6 compare fluctuation correlations of streamwise velocity and temperature, respectively. The comparison reveals that both profiles for M7.4-R4.1 are less sensitive to the grid refinements than M7.4-R6.4. Surprisingly, small variations of the fluctuation variance are observed away from the wall, with near-wall differences (see insets) resulting from different mean wall-shear and wall-heat flux values. This result indicates that the flow field in M7.4-R6.4 is also resolved well other than in the vicinity of the wall. The data from M7.4-LT4.1 also show the same trend in both the velocity and temperature fluctuations. Although the mesh of M7.4-LT4.1 is coarser than M7.4-R4.1, these grid sensitivity analyses indicate that the difference in the resolution influences only the near-wall behaviour. These correlations are almost independent of the grid resolution, and thus the performance of the present rescaling strategy can be fairly discussed by comparing M7.4-R4.1 and M7.4-LT4.1.

4. Volumetric rescaling methodology

In this section, the performance of the volumetric rescaling method is explored. For the examination, in §4.1 flow structures and turbulent spectra of the volumetric rescaling case M7.4-R4.1 are compared with those of the laminar-to-turbulent transitional case M7.4-LT4.1. Then, mean profiles and turbulent statistics are compared between the two cases to investigate the recovery length in the M7.4-R4.1 case in §4.2. The temperature–velocity relation during the recovery process is examined in §4.3. Finally, the effects of the rescaling box size are explored in §4.4.

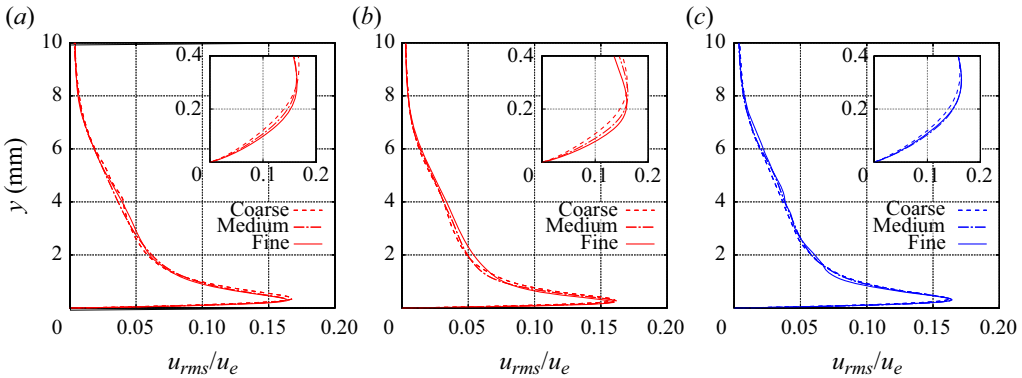


Figure 5. Grid sensitivity study for fluctuation correlations of streamwise velocity at $x = 0.85$ m in (a) M7.4-R4.1, (b) M7.4-R6.4 and (c) M7.4-LT4.1.

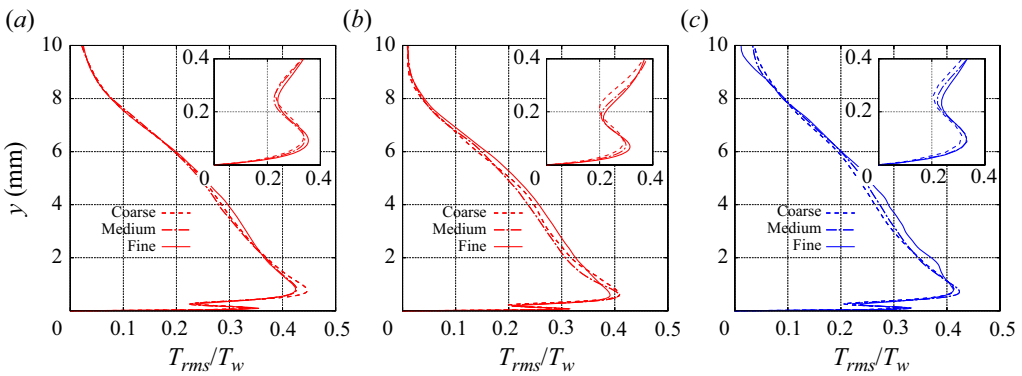


Figure 6. Grid sensitivity study for fluctuation correlations of temperature at $x = 0.85$ m in (a) M7.4-R4.1, (b) M7.4-R6.4 and (c) M7.4-LT4.1.

4.1. Comparison between volumetric rescaling and laminar-to-turbulent transition simulation

Figure 7 shows that the M7.4-LT4.1 case slightly underestimates the heat flux because its grid resolution is relatively coarse. The experimental data show a gradual transition to turbulence between $x = 0.3$ and 0.4 m, due to the presence of intermittent turbulent structures driven by a low-frequency component of the free-stream noise, which is correctly captured by M7.4-LT4.1. On the other hand, the SA model cannot account for the intermittency and therefore the precursor RANS profile suddenly jumps at $x = 0.3$ m. Since mean profiles at the inlet of the present rescaled LES are decided by the precursor RANS and fluctuations are extracted downstream where turbulence is fully developed, the effects of the intermittency are completely ignored in the rescaling simulation. Thus, computational domains of the rescaling cases need to be located sufficiently far from the turbulent transition location.

To examine if the selection of the computational domain is appropriate, figure 8 shows extracted fluctuations of streamwise velocity in the wall-parallel plane at $y = 0.5$ mm for M7.4-R4.1 and M7.4-LT4.1. In this paper, the streamwise direction is defined along the cone's surface as well as the x -direction. The region between $x = 0.6$ and 0.92 m in M7.4-LT4.1 is enlarged for comparison purposes. The comparison reveals that both cases

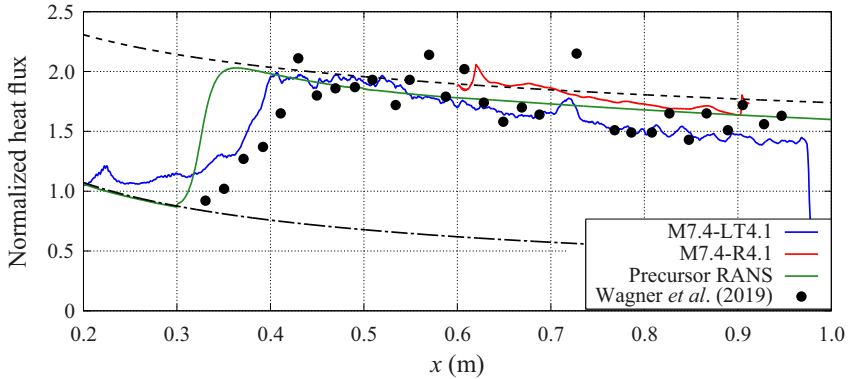


Figure 7. Comparison of wall-heat flux profiles between the volumetric rescaling simulation M7.4-R4.1 and the laminar-to-turbulent transition simulation M7.4-LT4.1. Data of the precursor RANS and the experiment by Wagner *et al.* (2019) are also included. Correlations for the laminar cone boundary layers (Lees 1956) and turbulent ones (White 2006) are given by dash-dotted and dashed lines, respectively.

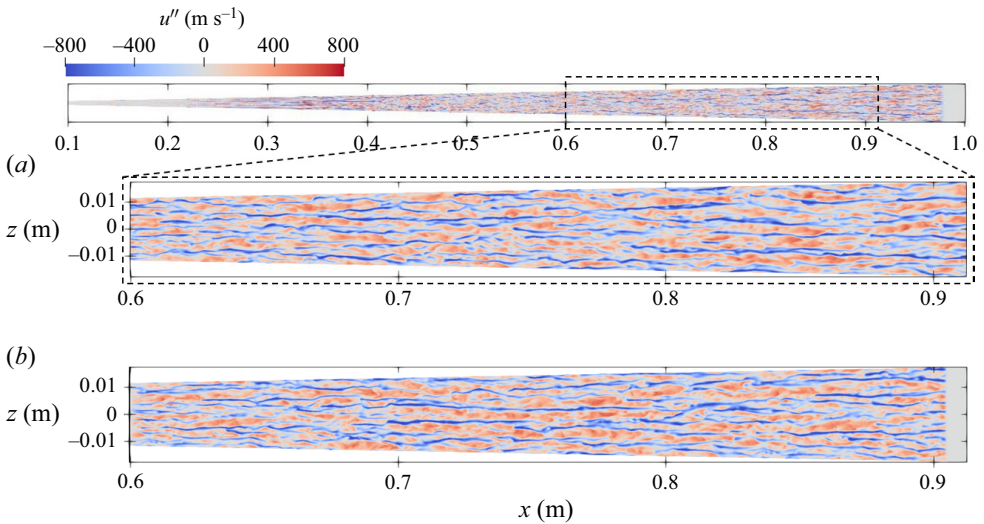


Figure 8. Comparison of velocity fluctuation fields in the wall-parallel planes at $y = 0.5$ (mm) between (a) the laminar-to-turbulent transition simulation M7.4-LT4.1 and (b) the volumetric rescaling simulation M7.4-R4.1.

have long streaky structures, with quite similar lengths and widths. This result implies that the effects of the turbulent intermittency do not reach $x = 0.6$ m, and the present rescaling method can generate similar flow fields to those of the laminar-to-turbulent transitional case in the fully turbulent region. Interestingly, the number of streaks in the azimuthal direction appears not to vary after $x = 0.6$ m with respect to x coordinates in the M7.4-LT4.1 case, and this is a quite important feature for the performance of the rescaling method. Since the extracted fluctuations are rescaled and recycled at the inlet, the energy spectra of imposed fluctuations should be almost the same as the extracted ones in the azimuthal direction. Therefore, the rescaling method should not be adopted to flow fields including strong variations in the streamwise direction. The almost invariable number of streaks in the laminar-to-turbulent transition case implies that variations of the flow field

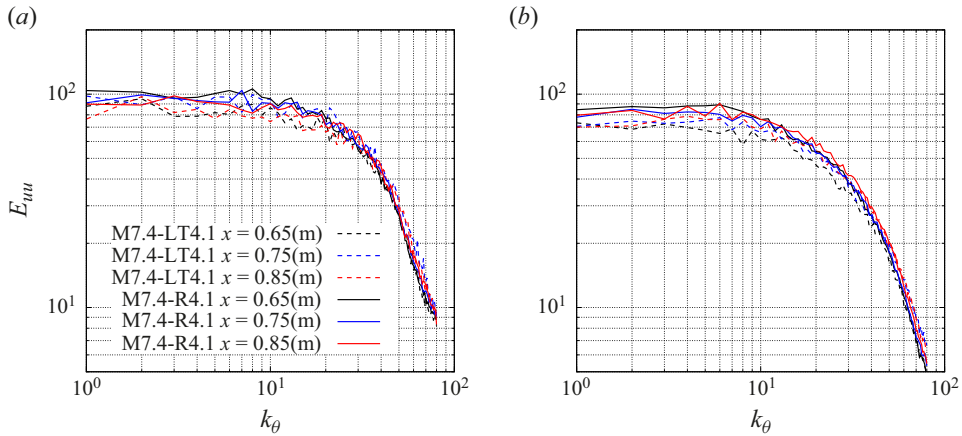


Figure 9. Comparison of one-dimensional spectra of streamwise velocity fluctuations in the azimuthal direction between the laminar-to-turbulent transition simulation M7.4-LT4.1 and the volumetric rescaling simulation M7.4-R4.1 for several x locations. The data are extracted at (a) $y^* = 15$ and (b) $y^* = 300$.

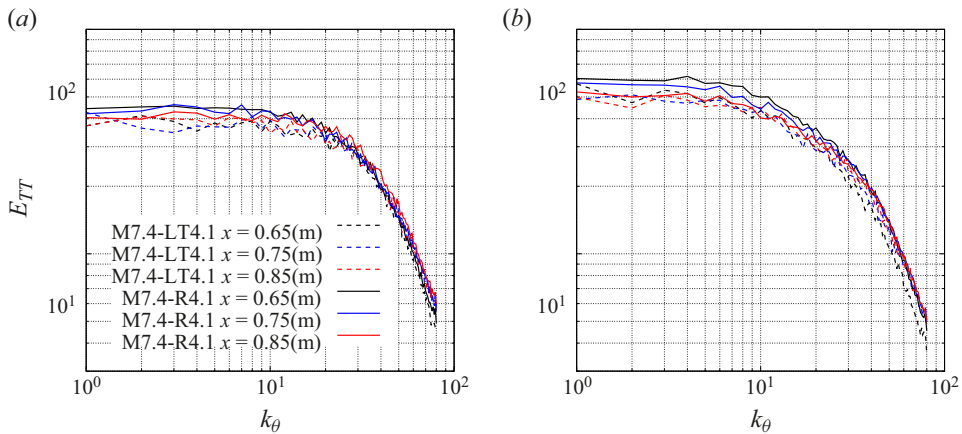


Figure 10. Comparison of one-dimensional spectra of temperature fluctuations in the azimuthal direction between the laminar-to-turbulent transition simulation M7.4-LT4.1 and the volumetric rescaling simulation M7.4-R4.1 for several x locations. The data are extracted at (a) $y^* = 15$ and (b) $y^* = 300$.

in the streamwise direction are moderate, and supports the applicability of the rescaling method to the current conical geometry.

Figures 9 and 10 show the azimuthal energy spectra of streamwise velocity and temperature fluctuations for the M7.4-R4.1 (rescaled) and M7.4-LT4.1 (fully transitional) cases. The spectra are extracted at $y^* = 15$ and $y^* = 300$ at three x locations. A negligible change in the streamwise direction is observed, and a good agreement is observed between M7.4-R4.1 and M7.4-LT4.1 at both y^* locations in general. This result is consistent with the observation of the velocity field in figure 8. A careful observation reveals that the streamwise velocity spectra for $y^* = 300$ show a larger value in the M7.4-R4.1 at a small wavenumber even at $x = 0.85$ m. The present rescaling calculations have a finer resolution than the fully transitional calculations, which leads to stronger fluctuations, hence a higher value of the spectral energy density, especially at the low wavenumbers. Upon closer inspection, the temperature spectra at $y^* = 300$ and $x = 0.65$ m of M7.4-R4.1

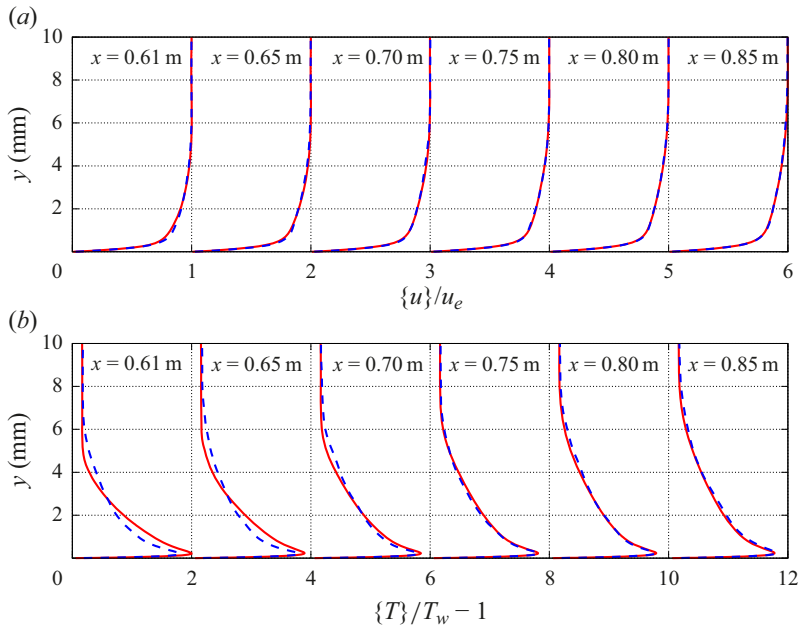


Figure 11. Mean profiles of (a) velocity and (b) temperature for $Re_m = 4.1 \times 10^6 \text{ m}^{-1}$ cases. Results of the volumetric rescaling simulation M7.4-R4.1 (red solid line) are compared with those of the laminar-to-turbulent transition simulation M7.4-LT4.1 (blue dashed line).

show a higher fluctuation intensity than M7.4-LT4.1 at the same location. The fluctuations in M7.4-LT4.1 depend on the upstream flow field affected by the laminar-to-turbulent transition process, while those in M7.4-R4.1 are obtained by recycling fluctuations from the downstream. Finally, at the most downstream location of $x = 0.85 \text{ m}$ (red lines), the spectra between both cases show the best agreement, indicating that the volumetric rescaling method can ultimately produce turbulent fluctuations with comparable structure to the case accounting for the full laminar-to-turbulent transition path.

4.2. Recovery length analysis

Since the mean profiles of the primitive variables in the present rescaling method are given by the RANS, a recovery process from the RANS profiles to real turbulent boundary profiles should occur immediately after the rescaling box. To examine the recovery length, figures 11 and 12 compare mean profiles and fluctuation correlations of velocity and temperature at several x locations between M7.4-R4.1 and M7.4-LT4.1. Profiles at $x = 0.61 \text{ m}$ are located at the centre of the rescaling box and other profiles are extracted at intervals of 0.05 m . Mean profiles and fluctuations of velocity are non-dimensionalized by the streamwise velocity at the edge of the boundary layer, and those of temperature by the wall temperature. The wall-normal coordinates are provided in mm to show the development of the boundary layer. The root mean squares (r.m.s.) of fluctuation correlations are computed by Favre average as

$$u_{i,rms} = \sqrt{\{u_i''u_i''\}}, \tag{4.1}$$

$$T_{rms} = \sqrt{\{T''T''\}}. \tag{4.2}$$

LES of conical hypersonic boundary layers

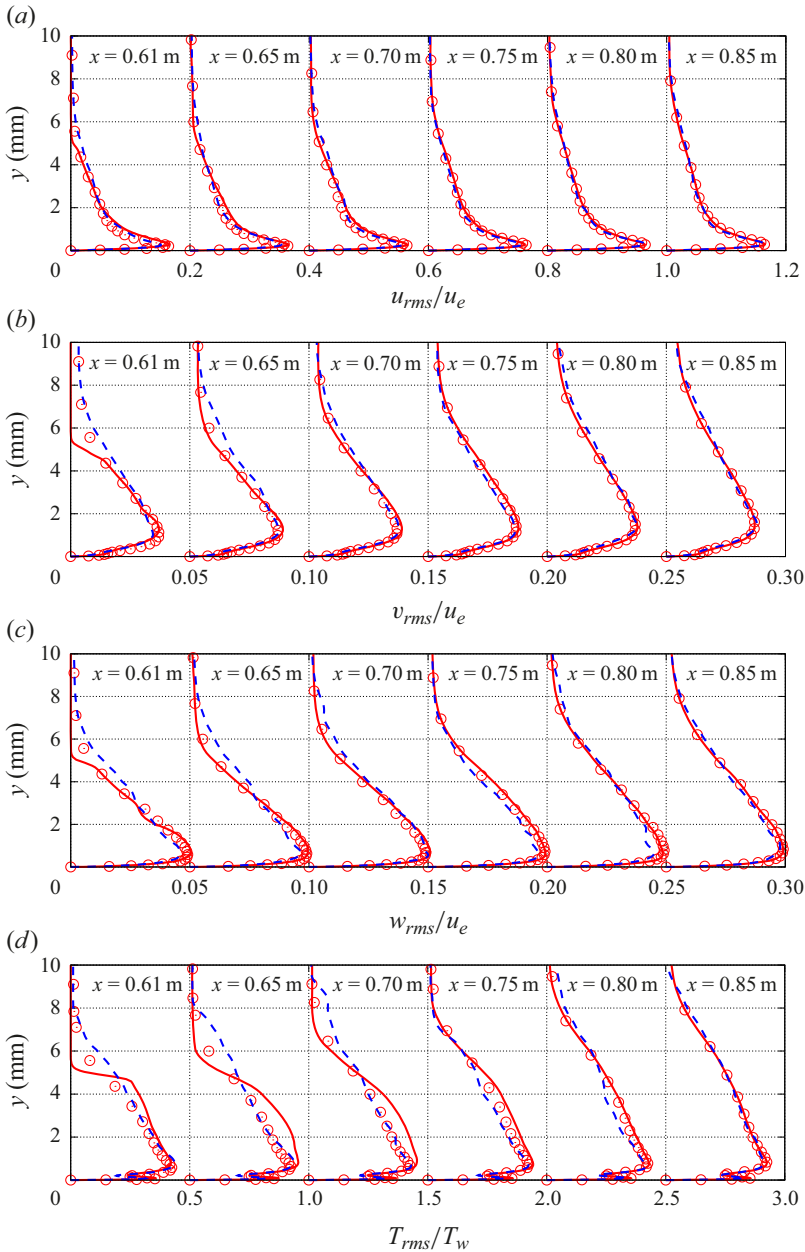


Figure 12. Fluctuation correlation profiles of (a) streamwise velocity, (b) wall-normal velocity, (c) spanwise velocity, (d) temperature for $Re_m = 4.1 \times 10^6 \text{ m}^{-1}$ cases. Results of the volumetric rescaling simulation M7.4-R4.1 (red solid line) are compared with those of the laminar-to-turbulent transition simulation M7.4-LT4.1 (blue dashed line). Red circles are the result of backpropagating the variance profiles from $x = 0.85$ to $x = 0.61$ m, rescaling them vertically based on the boundary-layer height, serving as a reference for the local self-similar state of turbulence.

Figure 11 shows that the mean velocity in M7.4-R4.1 agrees well with M7.4-LT4.1 even at $x = 0.61$ m, indicating that the SA model has a good prediction of the velocity profile, which is imposed on the rescaling box. As a result, the recovery length for

the mean velocity is very short in the present rescaling simulation. On the other hand, the mean temperature is different at the same location, indicating that the SA model has poor accuracy in the prediction of heat transfer in the hypersonic regime, and thus the temperature profile in the rescaling box deviates from that in the M7.4-LT4.1 case. However, the profile in the M7.4-R4.1 case becomes closer to the M7.4-LT4.1 case going downstream and collapses after $x = 0.75$ m. The agreement in the downstream indicates that the recovery length for the mean temperature is around 0.15 m.

By contrast, the fluctuation correlations in [figure 12](#) show several differences between M7.4-R4.1 and M7.4-LT4.1. Both the cases have similar profiles at $x = 0.85$ m, indicating that the boundary layer achieves an equilibrium state at this location independently of upstream flow history, also implying a self-similar state of the turbulent fluctuating field at that location. The red circles are obtained by backpropagating the turbulent fluctuating field statistical profiles, scaled by the local boundary-layer thickness, from $x = 0.85$ m to the inlet, serving as a reference for what the local state of equilibrium turbulence would look like. A procedural choice has been made in M7.4-R4.1, where fluctuations in the rescaling box (centred at $x = 0.61$ m) over $y = 5$ mm are suppressed, as mentioned in [§ 2.2](#).

The velocity variance profiles in M7.4-R4.1 agree well with the self-similar reference across the whole domain, while the temperature variance field departs from equilibrium immediately after the rescaling box at $x = 0.61$ and is the slowest among the variance profiles to relax to equilibrium, which is only achieved again after $x = 0.75$ m, where M7.4-R4.1 and M7.4-LT4.1 are equally far from the final self-similar state. We hypothesize that the present rescaling strategy suffers from the inaccuracy of the mean temperature profiles of the precursor RANS calculation.

The comparison of the mean profiles and fluctuation correlations revealed a recovery length for each variable, and all profiles in the M7.4-R4.1 case reach the equilibrium states after around $x = 0.8$ m. This result indicates that the volumetric rescaling method can generate reasonable turbulent flow fields over the cone geometry after a recovery length of 0.2 m, which is equivalent to 43δ based on boundary-layer thickness at the inflow.

The mean profiles in the present rescaling cases are given by the precursor RANS with the SA model and the comparison between the rescaling and laminar-to-turbulent cases revealed that a relatively long recovery length is required for the temperature. The recovery processes for both mean profiles and fluctuations depend on imposed mean profiles in the rescaling box. The SA model has poor accuracy in the prediction of heat transfer in hypersonic boundary layers (Aiken *et al.* 2022; Hendrickson *et al.* 2022) and thus, recent RANS models including modifications for compressible effects (McDaniel *et al.* 2016; Nichols 2019; Danis & Durbin 2022; Hendrickson *et al.* 2022; Parish *et al.* 2023; Chen *et al.* 2024; Xue *et al.* 2024) have potential to shorten the recovery length, especially as it pertains to the temperature variance field, when they are adopted for the precursor calculation. Wall-modelled LES (WMLES) for compressible boundary layers (Griffin, Fu & Moin 2023; Hendrickson *et al.* 2023) may also be a candidate for a precursor calculation, with the caveat that mean near-wall profiles in WMLES need to be reconstructed consistently with the model equation used for the inner layer.

4.3. Temperature–velocity relation during the recovery process

The analyses of the recovery length revealed that recovery of temperature is delayed, indicating that the present volume rescaling method requires a longer distance for the thermodynamic equilibrium than the hydrodynamic one. This result implies that the temperature–velocity relation varies during the recovery process. To examine the relation,

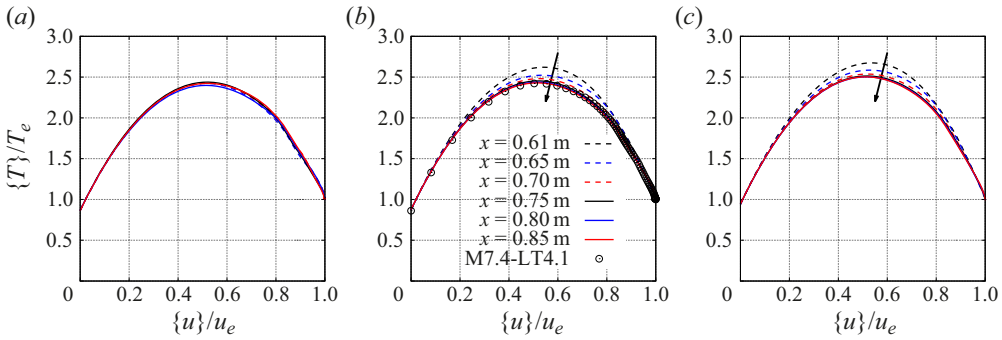


Figure 13. Temperature–velocity relation for (a) M7.4-LT4.1, (b) M7.4-R4.1 and (c) M7.4-R6.4 at several x locations. Black circles in (b) represent the M7.4-LT4.1 data at $x = 0.85$ m.

figure 13 provides the temperature–velocity relation for all cases, including the higher Reynolds number case M7.4-R6.4. The data for M7.4-LT4.1 are shown only after $x = 0.61$ m to discuss the fully turbulent region. The mean streamwise velocity and temperature in this figure are normalized by the edge values.

Interestingly, the data for M7.4-LT4.1 in figure 13(a) show excellent collapse, indicating that the temperature–velocity relation achieves self-similarity in the fully turbulent region. On the other hand, the data at $x = 0.61$ m of M7.4-R4.1 in figure 13(b) deviate from those of M7.4-LT4.1 because the mean temperature profile is largely different. However, the relation approaches the data of M7.4-LT4.1, going downstream and collapsing after $x = 0.75$ m, where the mean temperature showed a good agreement in figure 11. This result implies that the temperature–velocity relation becomes self-similar after the recovery process is completed. The relation for M7.4-R6.4 in figure 13(c) shows almost the same behaviour, indicating that the recovery process is also completed and thermodynamic equilibrium is achieved around $x = 0.75$ m in this case.

4.4. Effects of rescaling box size

As mentioned in § 2.3, the present rescaling method imposes fluctuations on the rescaling box for numerical stability of the spectral-like scheme. To investigate the effects of the rescaling box size on simulated flow fields, three different box sizes are tested under the condition of the M7.4-R4.1 case. The tested box sizes are summarized in table 3 and referred to as short, medium and long for simplicity. Coordinates at the beginning and the ending of the rescaling box where fluctuations are imposed, are indicated as x_{imp}^s and x_{imp}^e . Similarly, x_{ext}^s and x_{ext}^e are those of the recycling box, from which fluctuations are extracted. The parameter $L_{x,box}$ is the streamwise extent of the boxes in the x -direction. In all cases, $x_{imp}^s = 0.6$ m and $x_{ext}^s = 0.83$ m. The box sizes are changed in the x -direction: $L_{x,box} = 0.0095$ m for the short box, $L_{x,box} = 0.019$ m for the medium box and $L_{x,box} = 0.038$ m for the long box. The length of the medium box is generally applied in this paper. The lengths of the short and long boxes are half and double that of the medium one, respectively. The flow fields used in the analyses presented in this section are obtained using the coarse mesh $N_x \times N_y \times N_\theta = 960 \times 128 \times 84$ shown in table 2.

Figure 14 compares pressure fluctuation fields around the rescaling box in the streamwise wall-normal plane and the wall-parallel one to investigate the effects of the rescaling box size on numerical stability. The rescaling box is surrounded by the black

Case	x_{imp}^s (m)	x_{imp}^e (m)	x_{ext}^s (m)	x_{ext}^e (m)	$L_{x,box}$ (m)
Short box	0.6	0.6095	0.83	0.8395	0.0095
Medium box	0.6	0.619	0.83	0.849	0.019
Long box	0.6	0.638	0.83	0.868	0.038

Table 3. List of the tested rescaling box sizes.

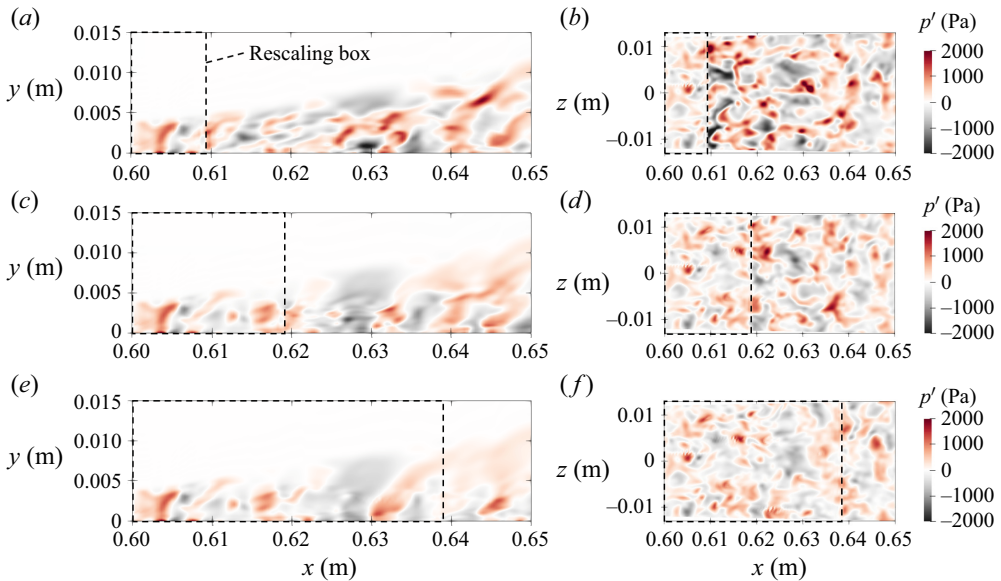


Figure 14. Pressure fluctuation fields around the rescaling box in (a,c,e) the streamwise wall-normal plane at the centre in the azimuthal direction, and (b,d,f) the wall-parallel plane at $y = 3.5$ mm. Panels show (a,b) short box, (c,d) medium box and (e,f) long box. The rescaling box is surrounded by the black dashed line box.

dashed line box. The pressure fluctuation with the short box intensifies immediately after the rescaling box. Since a shock wave should not exist in the present flow field, the strong pressure change is unphysical and it can induce numerical instability. The simulation with the short box cannot be sustained due to a numerical blow-up. The pressure fluctuation with the medium box is also strengthened after the rescaling box, however, its strength is so weak that the simulation is sustained. Moreover, the pressure field with the long box is smoothly connected even at the outlet of the rescaling box, indicating that the longer rescaling box can stabilize the simulation, as expected in § 2.3.

The non-physical pressure fluctuation after the rescaling box may severely affect flow fields downstream, and therefore the box size needs to be sufficiently long. On the other hand, the long rescaling box delays the recovery process from the RANS profiles, since the mean profiles in the rescaling box are fixed to the RANS ones. Thus, the shorter rescaling box is desirable from the perspective of the recovery length and the medium box is used in the present study. To investigate if the present box size is sufficient, wall-heat flux profiles and turbulent fluctuations are compared between the medium and long boxes in figure 15. Although small differences are observed around $x = 0.65$ m, the heat fluxes agree well with each other, and fluctuations of streamwise velocity and temperature show excellent collapses after $x = 0.7$ m. This result indicates that the effects of the rescaling box size

LES of conical hypersonic boundary layers

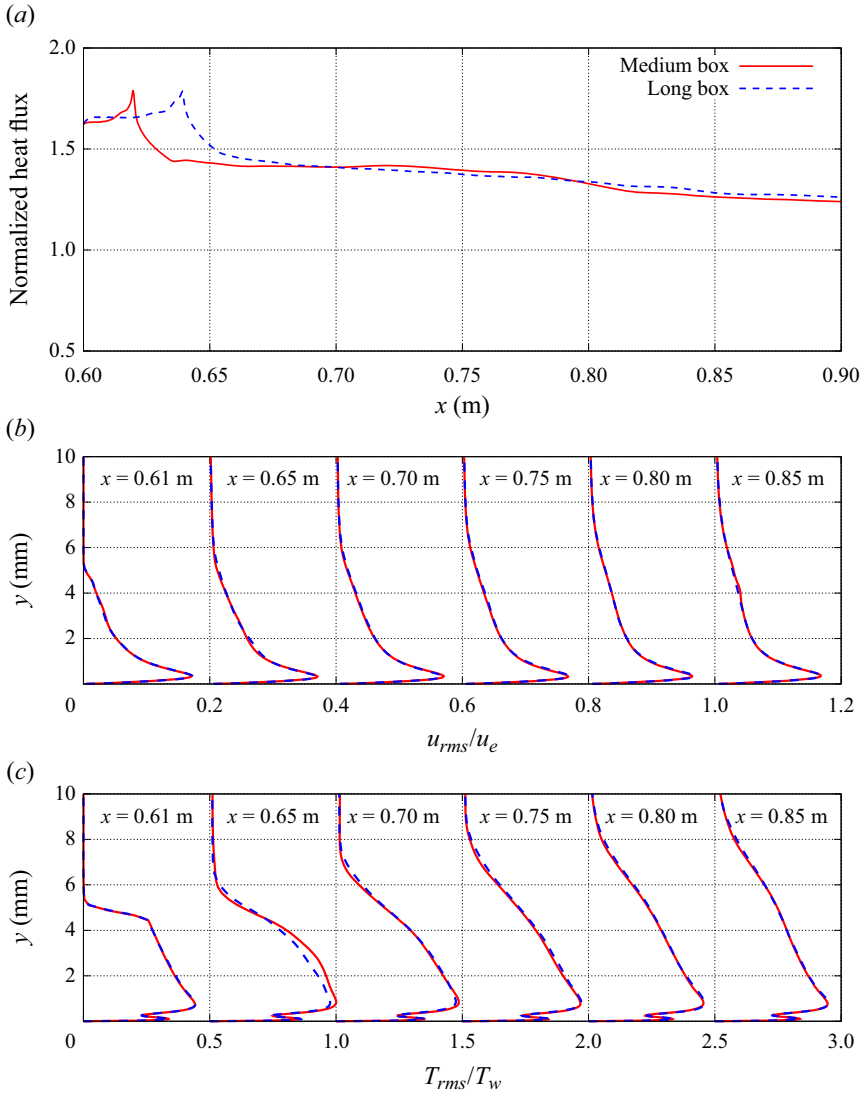


Figure 15. Comparison of (a) wall-heat flux, (b) fluctuation correlations of streamwise velocity and (c) fluctuation correlations of temperature between different rescaling box sizes.

do not extend to $x = 0.7$ m, and thus the medium box is sufficiently long to simulate the present conditions. In addition, the collapses imply that fluctuations after $x = 0.7$ are independent of the rescaling box, and therefore the recovery length is expected not to be influenced by the box size within the tested conditions.

The short box was also tested with the fine mesh $N_x \times N_y \times N_\theta = 1600 \times 256 \times 160$, and it numerically blew up as well (not shown). This result suggests that the minimum requirement for the rescaling box size is expected to depend on the size of flow structures rather than grid resolutions. The size of flow structures depends on several flow parameters, and therefore the optimal size of the rescaling box needs to be obtained by *a posteriori* study.

Correlation	r_g
Crocco–Busemann	1
Walz (1959)	r
Huang <i>et al.</i> (1993)	Pr_t
Duan & Martin (2011)	$r[a + (1 - a)(T_w - T_e)/(T_r - T_e)]$
Zhang <i>et al.</i> (2014)	$2C_p(T_w - T_e)/u_e^2 - 2Prq_w/(u_e\tau_w)$

Table 4. List of correlations for the temperature–velocity relation; $r \equiv (T_r - T_e)(T_0 - T_e)$ is the recovery factor. The turbulent Prandtl number is assumed to be 0.9 in Huang, Bradshaw & Coakley (1993) correlation. The parameter $a = 0.8259$ is given by the fitting of DNS data by Duan & Martin (2011).

5. Analysis of near-wall hypersonic turbulence structure

Since the analyses about the recovery length and rescaling box size clarified that the volumetric rescaling method is adequate to simulate the present conical hypersonic boundary layers, their flow dynamics is investigated in this section. First, the temperature–velocity relation in the equilibrium state is examined in § 5.1. Then, second-order statistics including the strong Reynolds analogy (SRA) are addressed in § 5.2. To examine the effects of the Reynolds number, the results of M7.4-R4.1 and M7.4-R6.4 are compared. Finally, attention is turned to instantaneous flow fields by visualizing velocity, temperature and density structures in § 5.3. The investigation focuses on the flow dynamics behind the turbulent statistics shown in § 5.2

5.1. Temperature–velocity relationship

Discussion in § 4.3 revealed that the temperature–velocity relation becomes self-similar in the equilibrium state. The estimation of the relation leads to the prediction technique of heat load at the wall, and thus several correlations have been proposed. Huang *et al.* (2022) listed correlations, which can be written as

$$\{T\} = T_w - \left(T_w - T_e - \frac{r_g}{2C_p} u_e^2 \right) \frac{\{u\}}{u_e} - \frac{r_g}{2C_p} \{u\}^2, \tag{5.1}$$

where the parameter r_g depends on each correlation, and they are summarized in table 4. According to Fernholz & Finley (1980), the Crocco–Busemann relation (Busemann 1931; Crocco 1932) is a classical correlation and Walz (1959) proposed an extended form by considering a recovery factor. Huang *et al.* (1993) derived their correlation by integrating the energy equation by assuming that the effective Prandtl number is equal to the turbulent Prandtl number in the viscous sublayer. Duan & Martin (2011) introduced the recovery enthalpy, and demonstrated that the enthalpy–velocity relation collapses, independently of free-stream Mach number. They derived the correlation parameter by the fitting of their DNS data and proposed the correlation by assuming a calorically perfect gas. Zhang *et al.* (2014) introduced a general recovery factor to modify Walz (1959) equation, and derived its value by considering the turbulent momentum and thermal transport in the wall-normal direction.

These correlations are applied to the present rescaled LES flow fields at $x = 0.85$, where the self-similarity is achieved, and compared in figure 16. Correlations of Crocco–Busemann, Walz (1959) and Huang *et al.* (1993) overestimate the temperature–velocity relation, while those of Duan & Martin (2011) and Zhang *et al.* (2014) show good agreements with the present rescaled LES. This result indicates that

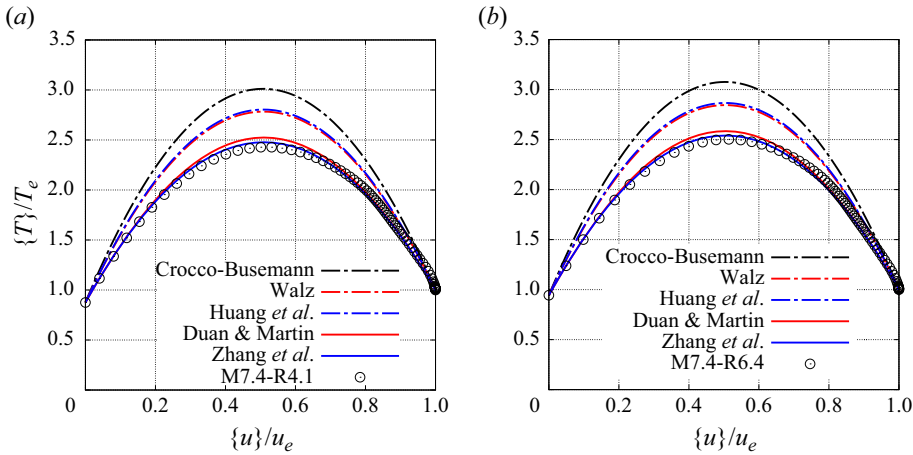


Figure 16. Comparison of temperature–velocity relation at $x = 0.85$ m between several correlations for (a) M7.4-R4.1 and (b) M7.4-R6.4.

these correlations can estimate the temperature–velocity relation reasonably well, although they were originally designed for flat plate boundary layers. Furthermore, the present wall-to-recovery temperature ratio is approximately 0.1, and figure 16 demonstrates that the temperature–velocity correlations of Duan & Martin (2011) and Zhang *et al.* (2014) remain applicable in such highly cooled hypersonic boundary layers.

5.2. Turbulent statistics

In this section, several turbulent statistics of the present rescaled LES in the wall-normal direction are shown. All data are extracted at $x = 0.85$ m since the recovery length analyses revealed that the recovering process is completed at this location.

Figure 17 provides profiles of velocity fluctuation correlations as a function of y/δ and y^* . The fluctuation correlations are semi-local scaled by mean density and shear stress at the wall. The DNS results of the Mach 11 hypersonic boundary layer on a flat plate for $Re_\tau = 1138$ by Huang *et al.* (2020) are also included in the figure. The velocity fluctuations in the present rescaled LES cases agree well with each other, indicating that velocity fluctuations over the cone geometry can be reasonably scaled in an existing way. The correlation of the streamwise velocity has the peak at almost the same location as the flat plate boundary layer, while the maximum value of the present rescaled LES is larger. Since an LES calculation does not fully resolve the turbulent dissipation field, streamwise velocity fluctuations are generally overestimated (Piomelli, Rouhi & Geurts 2015; Chapelier & Lodato 2016), especially with low-dissipation numerics, and the wall-shear stress underestimated. The correlations drop to almost 0 around $y^* = 2000$, whereas the flat plate data do not visibly decrease until $y^* = 300$. The discrepancy is attributed to variation in dynamic viscosity in the wall-normal direction. Both the present rescaled LES and the reference DNS have similar $Re_\tau \sim 10^3$ and the same wall temperature $T_w = 300$ K. By contrast, the free-stream temperature is largely different ($T_{\infty,DNS} = 66.5$ K and $T_{\infty,LES} = 248$ K or 268 K). The dynamic viscosity decreases toward the edge of the boundary layer in the reference DNS, as a result, Re_τ^* , which is computed based on wall shear stress and free-stream properties, is larger in the flat plate DNS ($Re_\tau^* \sim 10^4$) than the present rescaled LES ($Re_\tau^* \sim 10^3$), in spite of their similar

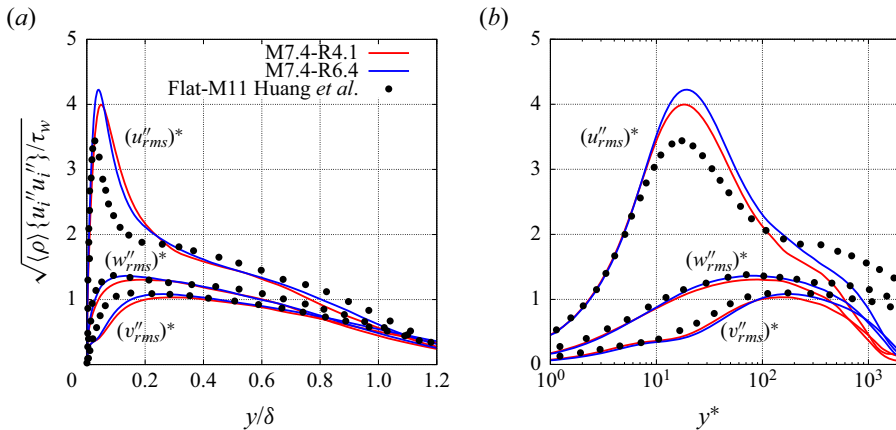


Figure 17. Velocity fluctuation correlations at $x = 0.85$ m as a function of (a) the outer scaling y/δ and (b) the semi-local wall unit y^* . The DNS results of flat plate hypersonic boundary layers by Huang *et al.* (2020) are also included.

$Re_\tau \sim 10^3$. Since y^* at the edge of the boundary layer is equal to Re_τ^* , the data of the present rescaled LES drop around $y^* = 2000$ whereas those of the reference DNS extend to the farther field.

Figure 18 compares present pressure fluctuation correlations with the incompressible boundary layer on a flat plate for $Re_\tau = 1145$ by Schlatter & Örlü (2010). The data in the present rescaled LES are larger than those in the incompressible one around the edge of the boundary layer. The pressure fluctuation in the incompressible flow is attributed to only hydrodynamics, whereas the shocklets also induce the fluctuation in the hypersonic flow. Since the shocklets can propagate over the boundary layer, substantial pressure fluctuation is observed around the edge. Besides, the data in the incompressible flow slightly decrease toward the wall, while those in the present rescaled LES increase below $y^* = 10$. This result indicates that strong pressure fluctuations, which are not observed in the incompressible flows, occur in the hypersonic boundary layers.

To explore the effects of the pressure fluctuations on thermodynamic properties, figure 19 shows fluctuation correlations of temperature and density, and figure 20 provides correlation coefficients among density, temperature and pressure. Both fluctuations in figure 19 have their maximum values at the plateau for $0.1 < y/\delta < 0.6$ and gradually decrease toward the far field. Additionally, both profiles have the second peak around $y^* = 5$. The temperature data drop toward the wall because of the iso-thermal boundary condition, while the density profile almost plateaus below $y^* = 5$. The density–temperature correlation coefficient $R_{\rho'T'}$ in figure 20 is around -0.8 over $y^* = 20$, indicating that the density and temperature are strongly anti-correlated over the buffer region. On the other hand, $R_{\rho'T'}$ gets close to 0 and the other correlations $R_{p'T'}$ and $R_{p'\rho'}$ become stronger below $y^* = 10$, indicating that temperature and density fluctuations are correlated to pressure in the vicinity of the wall. The profile in figure 18 showed strong fluctuations below $y^* = 10$, therefore the enhancement of the correlations $R_{p'T'}$ and $R_{p'\rho'}$ implies that the second peaks of temperature and density fluctuations around $y^* = 5$ are correlated to the strong pressure fluctuations near the wall. Effects of the strong pressure fluctuations are further discussed in § 5.3 by visualizing the pressure field at the wall.

Understanding the relationship between velocity and temperature is crucial for turbulence modelling, and in particular, many models are developed based on the SRA

LES of conical hypersonic boundary layers

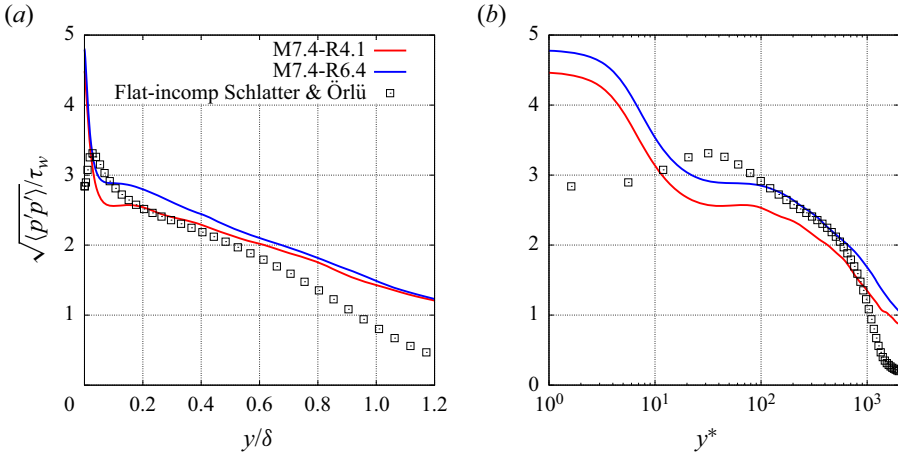


Figure 18. Pressure fluctuation correlations at $x = 0.85$ m as a function of (a) the outer scaling y/δ and (b) the semi-local wall unit y^* . The DNS results of flat plate incompressible boundary layers by Schlatter & Örlü (2010) are also included.

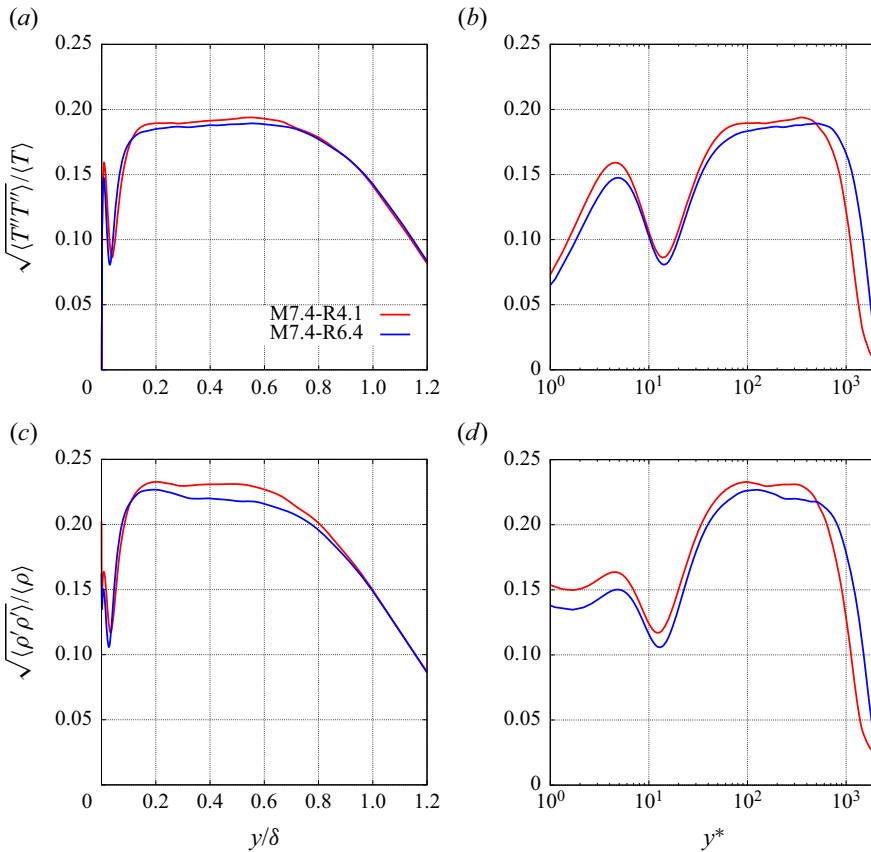


Figure 19. Fluctuation correlations of (a,b) temperature and (c,d) density at $x = 0.85$ m as a function of (a,c) the outer scaling y/δ and (b,d) the semi-local wall unit y^* .

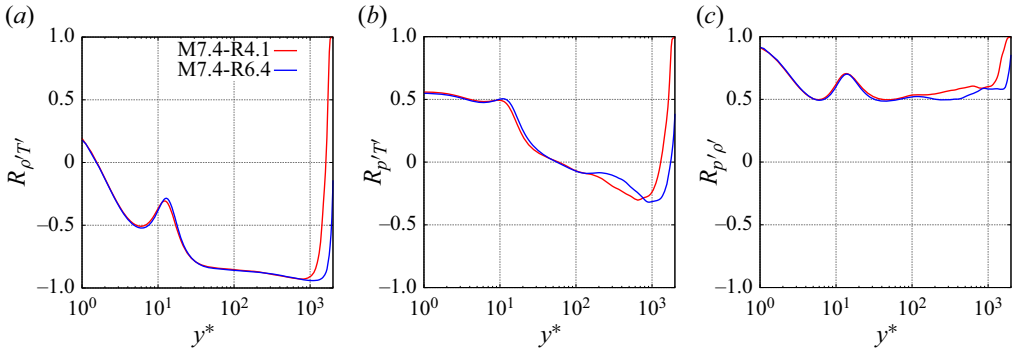


Figure 20. Correlation coefficients of (a) density–temperature, (b) pressure–temperature and (c) pressure–density at $x = 0.85$ m.

identified by Morkovin (1962). Assuming that the total temperature fluctuations are negligible, the SRA relation is derived for zero-pressure-gradient adiabatic turbulent boundary layers as

$$Pr_t = \frac{\langle \rho \rangle \{u'' v''\} (\partial \{T\} / \partial y)}{\langle \rho \rangle \{v'' T''\} (\partial \{u\} / \partial y)} \approx 1, \tag{5.2}$$

$$-R_{u'' T''} = -\frac{\{u'' T''\}}{\sqrt{\{u''^2\}} \sqrt{\{T''^2\}}} \approx 1, \tag{5.3}$$

$$\frac{\sqrt{\{T'' T''\}} / \{T\}}{(\gamma - 1) M^2 (\sqrt{\{u'' u''\}} / \{u\})} \approx 1, \tag{5.4}$$

where $M^2 = \{u\}^2 / (\gamma R_{gas} \{T\})$.

Figure 21 shows profiles of the turbulent Prandtl number Pr_t as a function of y/δ and y^* . The DNS data of the incompressible flat plate boundary layer (Li *et al.* 2009) and the hypersonic one (Huang *et al.* 2020) are also included. The value of Pr_t in the present rescaled LES slightly decreases for $y/\delta > 0.2$, and its qualitative trend is the same as the reference data. Since the temperature gradient becomes null in the buffer region, vertical fluid motions are not correlated to temperature fluctuations, and $\{v'' T''\}$ becomes null. As a result, Pr_t diverges around $y^* = 20$. In addition, Pr_t in the cone drops to 0.6 in the viscous sub-layer below $y^* = 3$. The comparison with the reference data revealed that such divergence and decrease are not observed in the incompressible boundary layer, but the hypersonic flat plate shows similar behaviours. Therefore, they are attributed to the hypersonic condition, and the turbulent Prandtl number over the hypersonic cone is qualitatively the same as the flat plate. Of note, such decrease of turbulent Prandtl number near the wall is not observable in subsonic wall-bounded flows including strong nonlinear density variations such as supercritical fluids (Kawai 2019; Toki, Teramoto & Okamoto 2020; Toki & Bellan 2021). Thus, the unique turbulent Prandtl number profile is expected to originate not from variation in density but from high Mach numbers.

Figure 22 provides the temperature–velocity correlation coefficient $-R_{u'' T''}$ as a function of y/δ and y^* . The value of $-R_{u'' T''}$ is almost -1 below $y^* = 5$, indicating that the velocity and temperature fluctuations are strongly correlated in the viscous sub-layer. Since the sign of the temperature gradient is switched in the buffer layer, the fluctuations become anticorrelated over $y^* = 50$. The maximum value of the coefficient is around 0.75 at

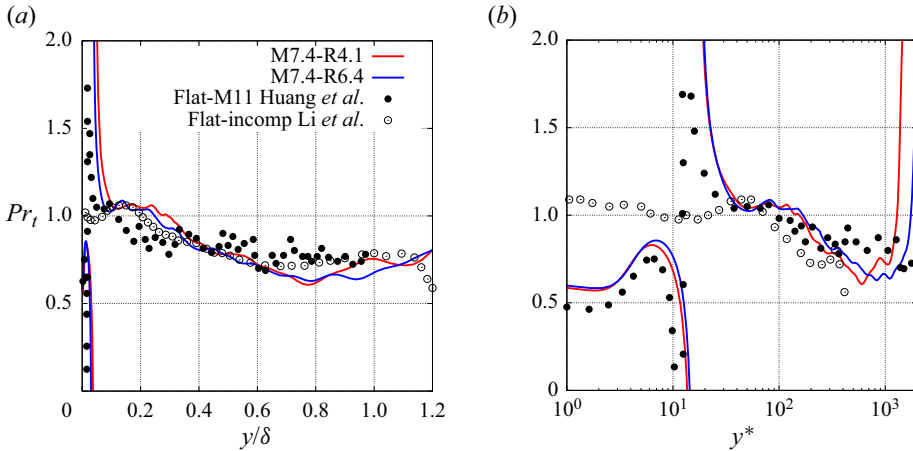


Figure 21. Turbulent Prandtl number at $x = 0.85$ m as a function of (a) the outer scaling y/δ and (b) the semi-local wall unit y^* . The DNS results of flat plate hypersonic boundary layers by Huang *et al.* (2020) and those of incompressible ones by Li *et al.* (2009) are also included.

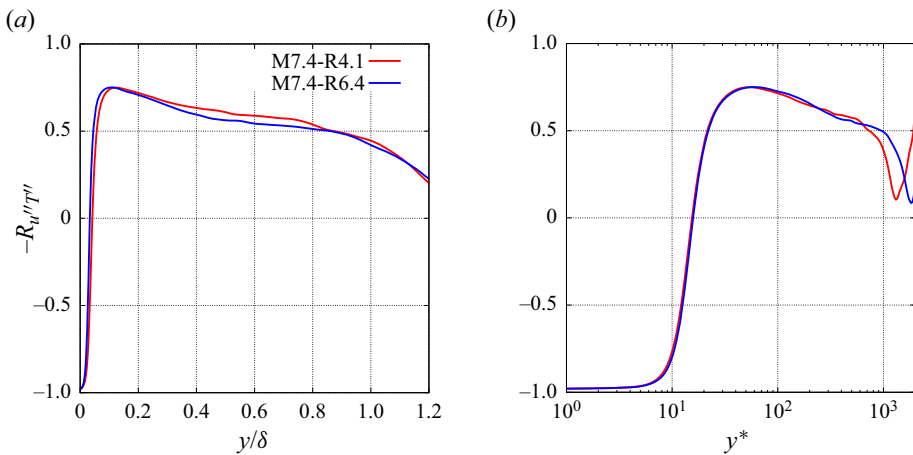


Figure 22. Temperature-velocity correlation coefficient at $x = 0.85$ m as a function of (a) the outer scaling y/δ and (b) the semi-local wall unit y^* .

$y/\delta = 0.1$ and it gradually decreases toward the far field. The imperfect correlation is also reported in a hypersonic flat plate boundary layer (Huang *et al.* 2022).

Figure 23(a) depicts the SRA relation of (5.4), and its value deviates from 1 in the entire boundary layer. The SRA relation is derived by neglecting the total temperature fluctuation, however, this assumption does not hold in the present condition because the total temperature varies in the wall-normal direction due to the extremely cold wall temperature. To account for the total temperature variation, Huang *et al.* (1995) modified the SRA by extending the velocity and temperature fluctuation relationship derived by Gaviglio (1987) and Rubesin (1990). Huang *et al.* (1995) SRA is generally referred to as HSRA and written as

$$\frac{\sqrt{\langle T'T' \rangle} / \langle T \rangle}{(\gamma - 1)M^2(\sqrt{\langle u'u' \rangle} / \langle u \rangle)} \left(1 - \frac{\partial \langle T_0 \rangle}{\partial \langle T \rangle} \right) Pr_t \approx 1, \quad (5.5)$$

where T_0 is the total temperature. The HSRA was developed for periodic channel flows, and therefore $\partial\langle T_0 \rangle / \partial\langle T \rangle$ considers only variations in the wall-normal direction. Following the original manner, the HSRA in this paper is computed as

$$\frac{\sqrt{\langle T'T' \rangle} / \langle T \rangle}{(\gamma - 1)M^2(\sqrt{\langle u'u' \rangle} / \langle u \rangle)} \left(1 - \frac{\partial\langle T_0 \rangle}{\partial y} \frac{\partial y}{\partial\langle T \rangle} \right) Pr_t \approx 1. \tag{5.6}$$

The HSRA is shown in [figure 23\(b\)](#). The fluctuation correlations and the derivative of the mean total temperature are computed based on the Reynolds-averaged value in Huang *et al.* (1995), however, it is sometimes computed based on the Favre-averaged ones (Duan *et al.* 2010; Passiatore *et al.* 2022). Thus, the HSRA is also computed with the Favre-averaged values as

$$\frac{\sqrt{\langle T''T'' \rangle} / \{T\}}{(\gamma - 1)M^2(\sqrt{\langle u''u'' \rangle} / \{u\})} \left(1 - \frac{\partial\{T_0\}}{\partial y} \frac{\partial y}{\partial\{T\}} \right) Pr_t \approx 1. \tag{5.7}$$

The HSRA of (5.7) is referred to as the Favre HSRA, and is shown in [figure 23\(c\)](#). Moreover, Zhang *et al.* (2014) added the modification of a turbulent Prandtl number to the HSRA as

$$\frac{\sqrt{\langle T'T' \rangle} / \langle T \rangle}{(\gamma - 1)M^2(\sqrt{\langle u'u' \rangle} / \langle u \rangle)} \left(1 - \frac{\partial\langle T_0 \rangle}{\partial y} \frac{\partial y}{\partial\langle T \rangle} \right) Pr_{t,zhang} \approx 1. \tag{5.8}$$

The modified turbulent Prandtl number is computed as

$$Pr_{t,zhang} = \frac{\langle (\rho v)'u' \rangle (\partial\langle T \rangle / \partial y)}{\langle (\rho v)'T' \rangle (\partial\langle u \rangle / \partial y)}. \tag{5.9}$$

The modified HSRA of (5.8) is referred to as Zhang’s HSRA and is depicted in [figure 23\(d\)](#). Since Zhang’s HSRA is defined by Reynolds-averaged values, its Favre-averaged version is also computed as

$$\frac{\sqrt{\langle T''T'' \rangle} / \{T\}}{(\gamma - 1)M^2(\sqrt{\langle u''u'' \rangle} / \{u\})} \left(1 - \frac{\partial\{T_0\}}{\partial y} \frac{\partial y}{\partial\{T\}} \right) Pr_{t,zhang} \approx 1. \tag{5.10}$$

This relation of (5.10) is referred to as Favre Zhang’s HSRA and is provided in [figure 23\(e\)](#). The modified turbulent Prandtl number $Pr_{t,zhang}$ is computed in the same manner as (5.9).

The HSRA shown in [figure 23\(b\)](#) shows improvements compared with the SRA, however, the profile monotonically decreases to 0.7 on going toward the boundary-layer edge ($y/\delta = 1.0$). Meanwhile, the Favre HSRA in [figure 23\(c\)](#) shows a similar trend to the HSRA, however, it drops to only 0.86 at $y/\delta = 1.0$, which is comparable to flat plate compressible boundary layers (Duan *et al.* 2010; Shadloo, Hadjadj & Hussain 2015; Huang *et al.* 2022). The improvement indicates that the computation based on the Favre average provides better results in the present highly cooled conical boundary layers. The same trend is observable for Zhang’s HSRA. The data obtained by Reynolds average in [figure 23\(d\)](#) decrease to 0.74, while Favre Zhang’s HSRA in [figure 23\(e\)](#) shows the best profile among the equations and it is 0.91 at $y/\delta = 1.0$.

A comparison between the M7.4-R4.1 and M7.4-R6.4 in [figures 17–23](#) reveals that the two cases show good agreements in all profiles. They have the same Mach numbers, but the higher Reynolds number is 1.5 times larger than the lower one. Therefore, the agreements indicate that the general turbulent statistics are almost independent of the Reynolds number as far as wall-normal coordinates are considered based on the outer scaling y/δ or the semi-local unit y^* within the present conditions.

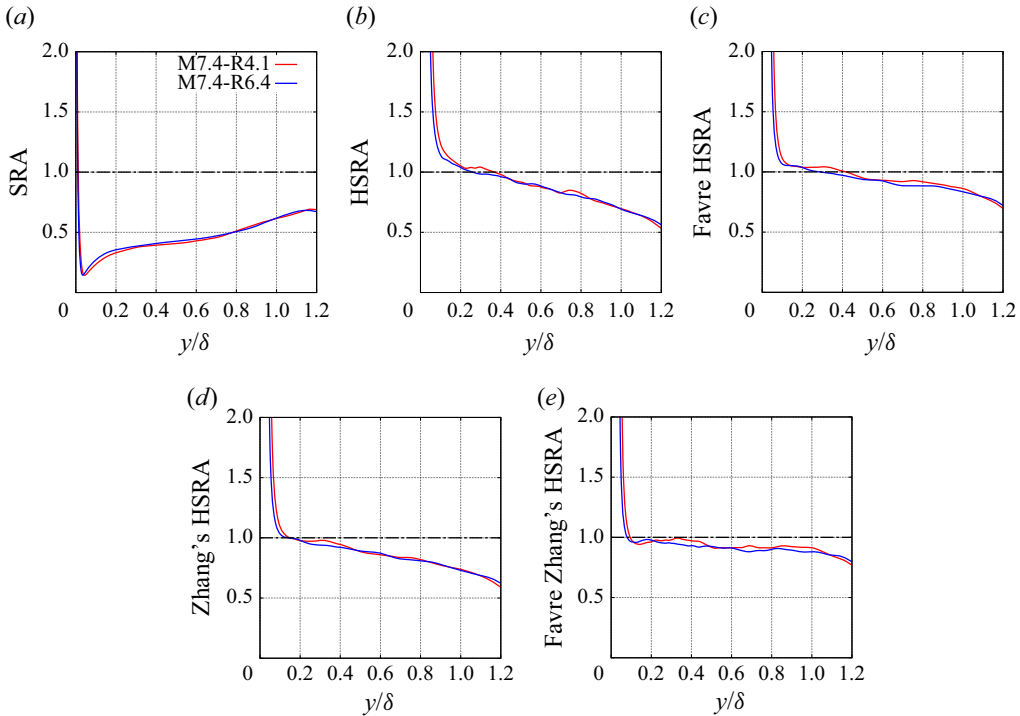


Figure 23. (a) The SRA relation of (5.4), (b) the HSRA of (5.6), (c) the Favre HSRA of (5.7), (d) Zhang's HSRA of (5.8) and (e) the Favre Zhang's HSRA of (5.10) at $x = 0.85$ m.

Finally, most obtained statistics are consistent with the referred to flat plate boundary layers in spite of the conical geometry. The consistency with the flat plates implies that the effects of azimuthal expansion are small in the current simulated region. The effects are the most significant around the tip, however, the boundary layer should be laminar until the turbulent transition occurs. Since the transitional point is shifted upstream as an increase in the Reynolds number (Sousa *et al.* 2024), the effects of the conical geometry on turbulence are expected to be pronounced in higher Reynolds number flows.

5.3. Flow structure

To understand instantaneous flow structures, fluctuation data of u , T and ρ are extracted at various distances from the wall for the M7.4-R4.1 case in figures 24–26. Figure 24 shows fluctuations at $y = 0.064$ mm ($y/\delta = 0.01$, $y^* = 5$ at $x = 0.85$ m), which are representative of the near-wall region. Figure 25 illustrates data at $y = 1.9$ mm ($y/\delta = 0.3$, $y^* = 160$ at $x = 0.85$ m), which correspond to the inner layer. Figure 26 depicts information at $y = 5.6$ mm ($y/\delta = 0.9$, $y^* = 760$ at $x = 0.85$ m), which is located around the edge of the boundary layer. Furthermore, figure 27 provides two-point streamwise correlations of u , T and ρ in the streamwise and azimuthal directions at various extracted y locations centred at $x_{ref} = 0.8$ m to discuss the statistical size of the boundary-layer structures. The correlation data in the streamwise direction are extracted in both the upstream and downstream directions; the azimuthal direction is periodic, so only positive displacements in the curvilinear coordinate z are shown. Since the present boundary layer is spatially developing, the absolute distance from the wall of a given y^* plane may vary

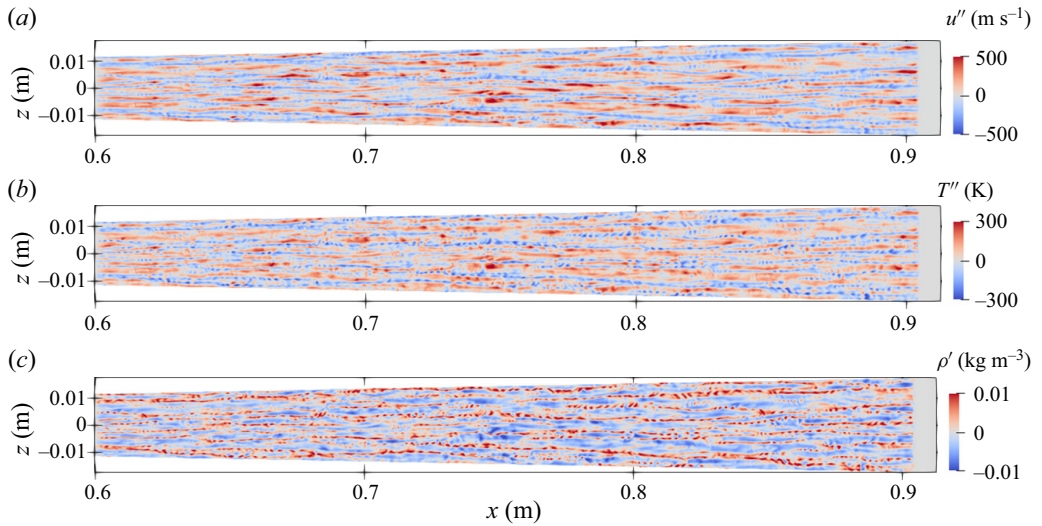


Figure 24. Instantaneous snapshot in the $y = 0.064$ mm ($y/\delta = 0.01$, $y^* = 5$ at $x = 0.85$ m) wall-parallel plane for M7.4-R4.1. Statistical fluctuation of (a) streamwise velocity, (b) temperature and (c) density.

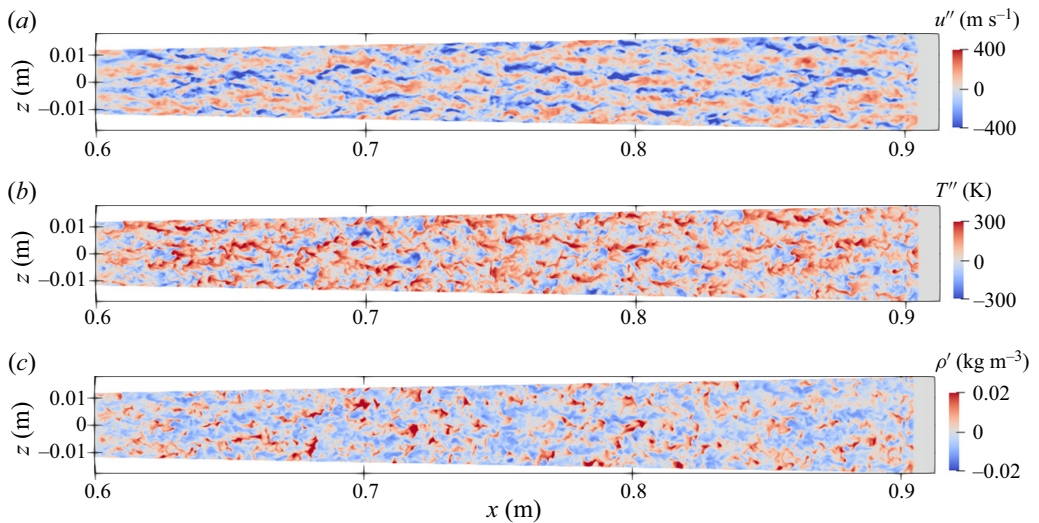


Figure 25. Instantaneous snapshot in the $y = 1.9$ mm ($y/\delta = 0.3$, $y^* = 160$ at $x = 0.85$ m) wall-parallel plane for M7.4-R4.1. Statistical fluctuation of (a) streamwise velocity, (b) temperature and (c) density.

largely in the streamwise direction. Flow structures depend on the y^* value rather than the physical wall-normal distance, and thus the correlations are computed for each y^* plane. Flow structures in the higher Reynolds number case M7.4-R6.4 were also examined, however, its structures are quite similar to the M7.4-R4.1 case, and thus they are not displayed in this paper.

The velocity field at $y = 0.064$ mm in [figure 24](#) shows streaky structures, which have quite thin spacing in the azimuthal direction and a long one in the streamwise direction. Coleman, Kim & Moser (1995) reported that turbulent structures in the supersonic channel flows are elongated in the streamwise direction, and Duan *et al.* (2010) clarified that

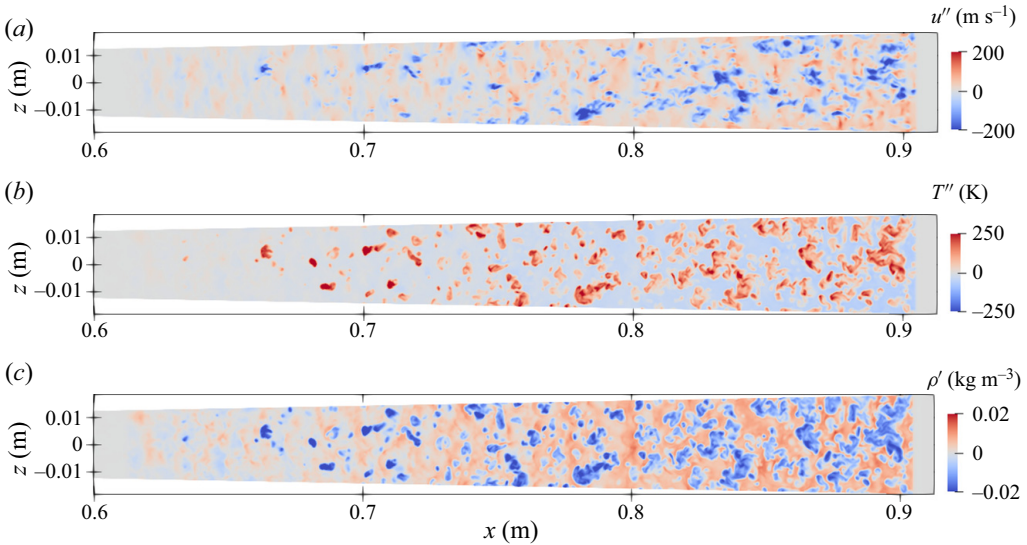


Figure 26. Instantaneous snapshot in the $y = 5.6$ mm ($y/\delta = 0.9$, $y^* = 760$ at $x = 0.85$ m) wall-parallel plane for M7.4-R4.1. Statistical fluctuation of (a) streamwise velocity, (b) temperature and (c) density.

the low wall-to-recovery temperature ratio decreases spanwise meandering and increases streamwise coherency in hypersonic boundary layers. The observed long structures in the cone boundary layer are consistent with these past findings. In addition, the present wall-to-recovery temperature ratio is reduced to around 0.1, which is lower than the referred to studies, therefore, the straightness of the streaks is expected to be enhanced. The two-point correlation for u in figure 27(a,b) shows that the correlation does not drop to 0 until $(x - x_{ref})/\delta = 9$, while the data drop quickly toward $z/\delta = 0.14$ in the azimuthal direction, indicating that the streamwise spacing is approximately 65 times longer than the azimuthal one. The temperature field at this location has quite similar structures to the velocity. The temperature–velocity correlation coefficient $-R_{u''T''}$ in figure 22 was almost -1 below $y^* = 5$, and the observed similarity supports the strong correlation. Careful observation reveals that the temperature locally fluctuates in the streamwise direction with short wavelengths, and interestingly, the fluctuations exist only in low-temperature streaks. Since the mean temperature increases from the wall at this y location, low-temperature fluids should originate from the vicinity of the wall. In turbulent boundary layers, upward motions transport the near-wall fluids, and such behaviours are known as ejection events. Temperature streaks attributed to ejection events are observable in supersonic boundary layers (Pirozzoli & Bernardini 2011) and subsonic ones with a temperature gradient (Toki & Bellan 2021, 2022), and thus the present low-temperature streaks are expected to be accompanied by ejection events in the same manner as the referred to boundary layers. By contrast, the short-wavelength fluctuations in the temperature streaks were not observed in such boundary layers, implying that these phenomena are attributed to the present hypersonic conditions. The density reflects the temperature field since they are coupled with the equation of state. High-density streaks are correlated to the low-temperature streaks, and *vice versa*. Similarly to the temperature, strong fluctuations are observed in the high-density streaks.

The velocity field at $y = 1.9$ mm in figure 25 shows that the streamwise spacing of both low- and high-speed velocity streaks is shorter and the spanwise spacing is wider than

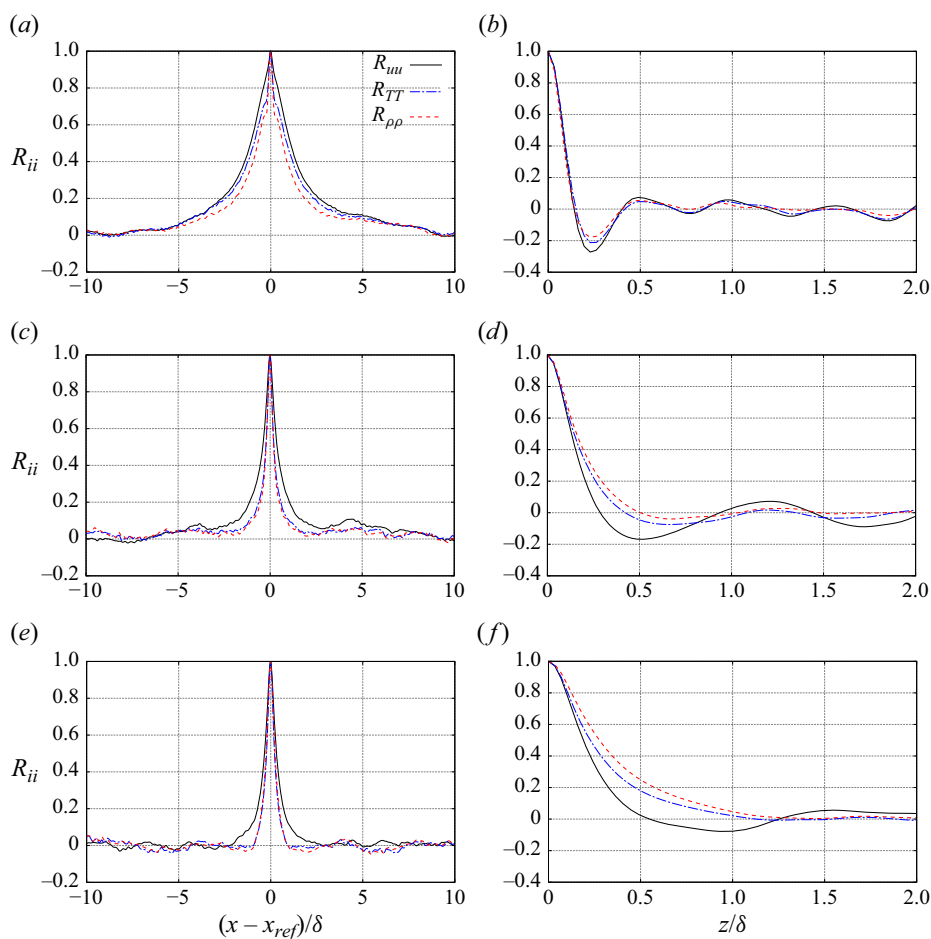


Figure 27. Two-point correlations of streamwise velocity, temperature and density components at $x_{ref} = 0.8$ m in the (a,c,e) streamwise and (b,d,f) azimuthal directions. The data are computed for (a,b) $y^* = 5$, (c,d) $y^* = 161$ and (e,f) $y^* = 784$. These y^* locations correspond to (a,b) $y = 0.064$ mm, (c,d) $y = 1.9$ mm and (e,f) $y = 5.6$ mm, respectively.

those at $y = 0.064$ mm. This observation is supported by the two-point correlation shown in figure 27(c,d). Since the mean temperature gradient is switched around $y = 0.23$ mm ($y/\delta = 0.037$) as shown in figure 11, the high-temperature streaks can be observed at the same locations of low-speed streaks. The anti-correlation is consistent with $-R_{u''T''}$ in figure 22. In contrast, low-temperature streaks are not clear despite the clear high-velocity streaks. This result indicates that the weak anti-correlation between the velocity and temperature in figure 22 is attributed to downward vertical motions (sweep events) because the mean temperature decreases toward the far field. In addition, the two-point correlations of temperature indicate shorter and wider structures than the streamwise velocity field. The dissimilarity was also observed in supersonic and subsonic boundary layers (Pirozzoli & Bernardini 2011; Toki & Bellan 2021, 2022). The temperature fluctuations observed in the near-wall low-temperature streaks do not exist in this plane, indicating that they only appear in the vicinity of the wall. The density field reflects the temperature field, similarly to the near-wall region. Since the density is inversely proportional to the temperature, low-density streaks are clear while high-density streaks are not clearly observable.

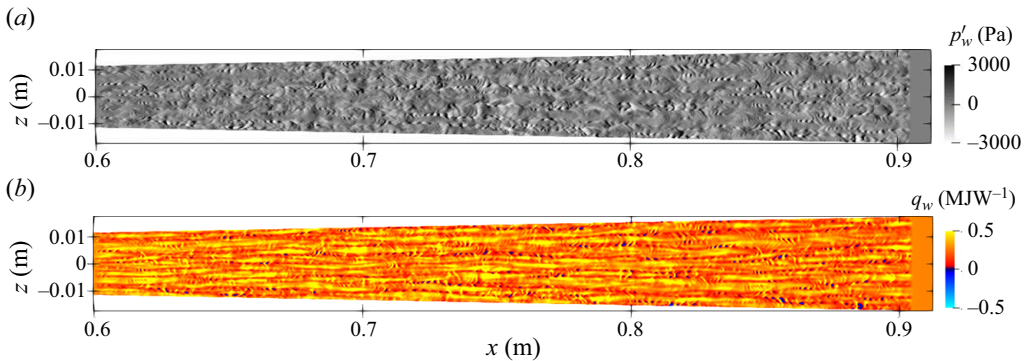


Figure 28. Instantaneous snapshot at the wall for M7.4-R4.1: (a) pressure fluctuation and (b) wall-heat flux.

At $y = 5.6$ mm, streaks no longer exist in any contours, and the two-point correlations quickly drop to 0 in the streamwise direction for all components. Fluctuations are quite weak in the upstream before $x = 0.65$ m because the edge of the boundary layer does not reach this plane. The similarity between the velocity and temperature becomes further obscure, which is consistent with the low $-R_{u''T''}$ in figure 22. Some high-temperature and low-density fluctuations are shaped akin to a mushroom-like structure reported in supersonic boundary layers by Pirozzoli & Bernardini (2011) despite the present hypersonic Mach number.

Some features in the inner and outer layers are similar to supersonic and subsonic boundary layers, whereas the strong fluctuations in low-temperature streaks in the vicinity of the wall have not been reported in such boundary layers. In addition, pressure fluctuations shown in figure 18 are enhanced near the wall, and thus a straightforward expectation is that the hypersonic condition induces the strong pressure fluctuations, and the temperature ones result from them. To further investigate the near-wall phenomenon, figure 28 shows instantaneous contours of pressure fluctuations at the wall. Moreover, the wall-heat flux contour is also included to investigate the effects of the temperature fluctuations on the heat load at the wall.

The wall-pressure fluctuation field shows strong pressure oscillations in the streamwise direction. A careful comparison with the near-wall temperature fluctuation in figure 24(b) clarifies that the pressure oscillations are correlated to the temperature fluctuations. This observation is consistent with the near-wall behaviour of the pressure–temperature correlation in figure 20. Similar pressure oscillations were originally observed in supersonic and hypersonic channel flows, and they are called alternating positive and negative structures by Tang *et al.* (2020) or trapped waves by Chen & Scalo (2021b). Similar pressure structures were also recently observed in hypersonic boundary layers by Xu, Wang & Chen (2023) and Huang *et al.* (2024). Following Chen & Scalo (2021b), we call the pressure oscillations a trapped wave in this paper. Chen & Scalo (2021b) mentioned the possibility that the trapped wave resembles the amplification of second-mode waves in cooled hypersonic boundary layers, in which an enhancement in wall cooling yields a stronger instability in the hypersonic laminar boundary-layer flow. Research about the instability, which is summarized in Fedorov (2011), revealed that acoustic rays are trapped between the wall and the sonic line owing to the presence of a region of supersonic mean flow relative to the disturbance phase velocity. The observation of figures 24(b) and 28(a) clarifies that the trapped waves exist only in fluids ejected from

the wall, implying that the waves are induced by the interaction between the boundary layer and the wall as well as the second-mode waves.

Effects of the trapped waves extend to the wall-heat flux shown in [figure 28\(b\)](#). The trapped waves involve strong fluid expansion and compression, and therefore strong and localized temperature fluctuations also occur near the wall, as shown in [figure 24\(b\)](#). Since the wall-heat flux reflects the near-wall temperature field, its structures are similar to those of the temperature. The heat flux field has streaky structures and oscillating patterns attributed to the trapped waves are also observed, indicating that the trapped waves induce strong fluctuations of wall-heat flux. Similar structures of wall-heat flux and wall-shear stress were also reported for hypersonic boundary layers over flat plates by Roy *et al.* (2024). In addition, the fluid temperature locally becomes below the wall temperature in the vicinity of the wall due to the strong fluid expansion. As a result, the wall-heat flux shows local negative values, indicating that the boundary layer locally absorbs heat from the wall against the statistical direction.

For further investigation, [figure 29](#) shows a time series of the pressure fluctuations at the wall for $0.76 \text{ m} \leq x \leq 0.84 \text{ m}$ and $-0.014 \text{ m} \leq z \leq 0 \text{ m}$. The x and z coordinates are normalized by the wall viscous length scale $l^+ \equiv \mu_w / \sqrt{\rho_w \tau_w}$ at $x_{ref} = 0.8 \text{ m}$. The instantaneous snapshots are extracted at 7 different times t every $4.8 \mu\text{s}$. A selected series of trapped waves is surrounded by the white dashed line square box at each t to explore its propagation. The fluctuation profiles along the white dash-dotted line are also shown in [figure 30](#). Fluctuations of wall-heat flux are included as well and the extracted fluctuations are non-dimensionalized by local mean values. A wavelength in the streamwise direction λ_x^+ is estimated based on a distance between positive peaks and included. The wavelength is also normalized by l^+ .

The trapped waves in the box of the white dashed line propagate in the streamwise direction. The extracted pressure profile in [figure 30\(a\)](#) shows that the strength of the fluctuation is around 50 % of the local mean pressure and λ_x^+ is around 300 at $t = 0 \mu\text{s}$. The pressure fluctuation reaches 100 % of the local mean pressure, and λ_x^+ is reduced to 225 at $t = 9.6 \mu\text{s}$. After that, λ_x^+ gradually increases to around 570 as t progresses, and the selected trapped waves almost disappear at $t = 28.8 \mu\text{s}$. The observation of the time history implies that their wavelength is approximately 200 to 600 times as long as the wall viscous length scale l^+ , which is around $5 \mu\text{m}$. The boundary-layer thickness δ is 5.9 mm at $x_{ref} = 0.8 \text{ m}$, and therefore the wavelength is around 0.17 to 0.5δ . In addition, the series of trapped waves travel around $9000l^+$ during $28.8 \mu\text{s}$ and disappears. This length corresponds to $0.045 \text{ m} \sim 7.6\delta$ and their travel speed is around 1560 ms^{-1} corresponding to Mach 4.5 based on the wall temperature. The frequency of the trapped waves can be estimated as between 520 and 1560 kHz from the speed and wavelength. The short travel distance indicates that the trapped waves repeat appearances and disappearances, and do not circulate by the rescaling method. Furthermore, the occurrence of the trapped waves indicates that the second-mode instability in the hypersonic regime is important even in turbulent states.

Profiles of wall-heat flux fluctuations in [figure 30](#) display a high degree of correlation with the wall-pressure fluctuations, supporting the idea that the aforementioned trapped waves may be responsible for the strong overshoots in the wall-heat flux, which may reach two times the mean (e.g. see $t = 14.4 \mu\text{s}$). Pressure fluctuations are dominated by inviscid mechanisms and follow the wave propagation velocity. By contrast, fluctuations of wall-heat flux depend on the temperature of the near-fluid parcels, regulated by convective wall-normal transport mechanisms, ultimately limited by molecular diffusion in the thermal sublayer. This correlation is surprising since trapped waves seem to exist only

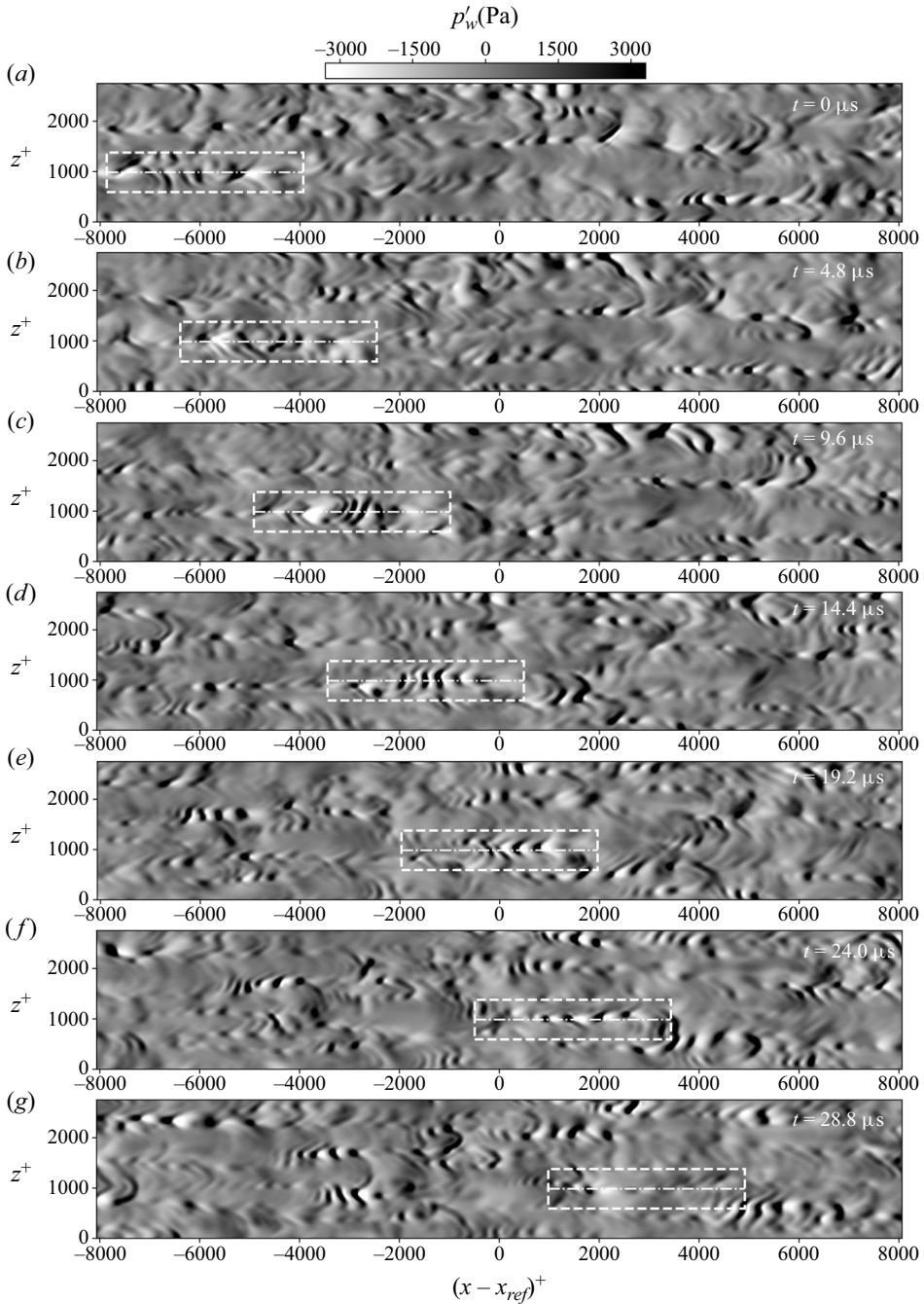


Figure 29. Contours of pressure fluctuations at the wall in M7.4-R4.1 at (a) $t = 0 \mu\text{s}$, (b) $t = 4.8 \mu\text{s}$, (c) $t = 9.6 \mu\text{s}$, (d) $t = 14.4 \mu\text{s}$, (e) $t = 19.2 \mu\text{s}$, (f) $t = 24.0 \mu\text{s}$ and (g) $t = 28.8 \mu\text{s}$. A selected series of trapped waves is surrounded by the white dashed line square box at each t to explore its propagation. Profiles of pressure fluctuations along the white dash-dotted lines are extracted and shown in [figure 30](#).

in regions of fluid ejection (see [figure 24](#)), which is responsible for negative fluctuations in heat flux. However, this does suggest that the trapped waves are responsible for regulating the convective supply of colder or hotter (than the wall) fluid parcels at the edge of the

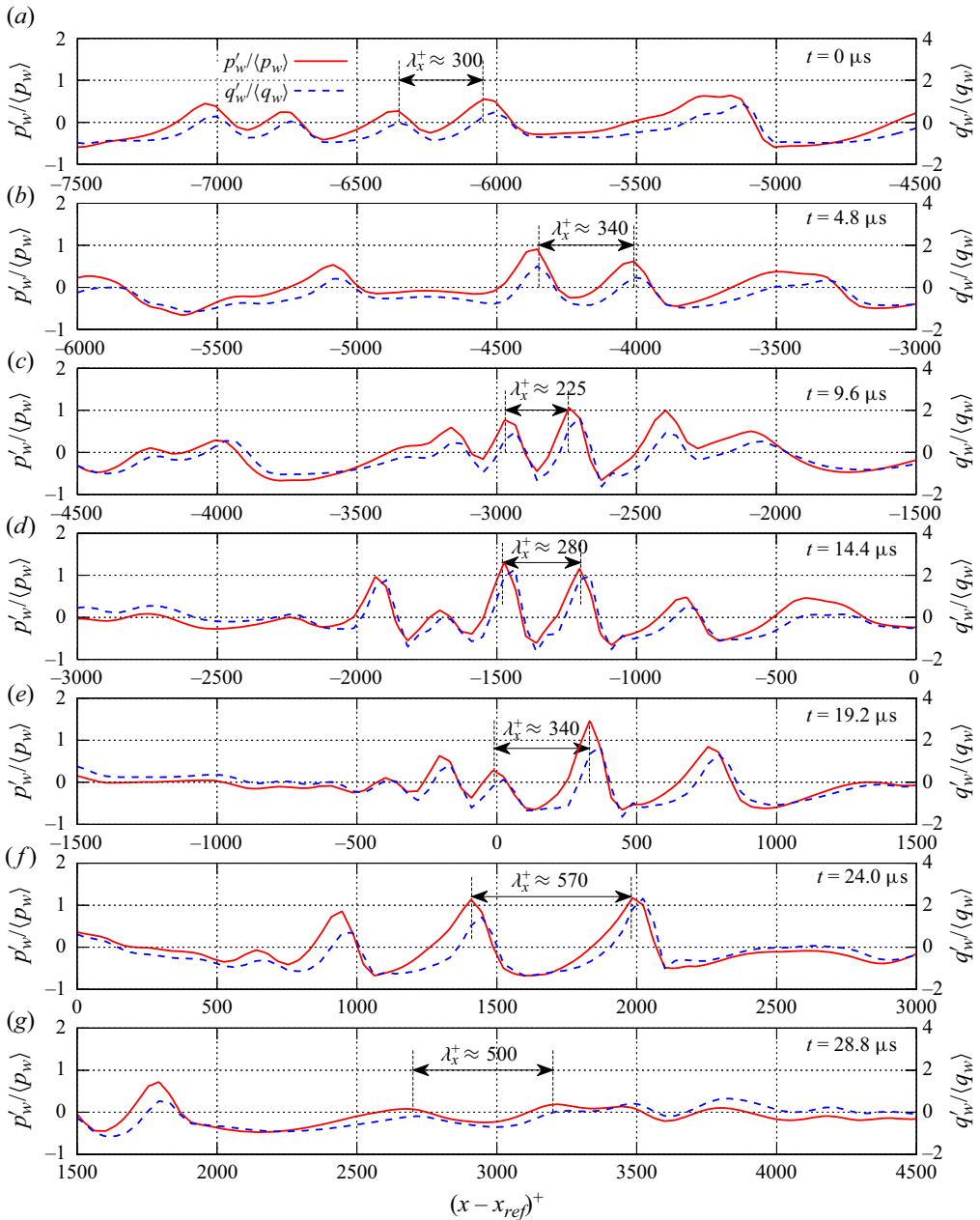


Figure 30. Profiles of pressure and wall-heat flux fluctuations at the wall along the white dashed-dotted lines in figure 29 at (a) $t = 0 \mu s$, (b) $t = 4.8 \mu s$, (c) $t = 9.6 \mu s$, (d) $t = 14.4 \mu s$, (e) $t = 19.2 \mu s$, (f) $t = 24.0 \mu s$ and (g) $t = 28.8 \mu s$.

thermal sublayer. More investigation into this phenomenological correlation is warranted and deferred to future studies.

Figure 31 extracts the pressure fluctuation field below $y^+ = 150$ in the (x, y) plane along the dashed-dotted lines in the middle of the dashed white boxes in figure 29 to investigate structures of the trapped waves in the wall-normal direction. Contour lines of local Mach

LES of conical hypersonic boundary layers

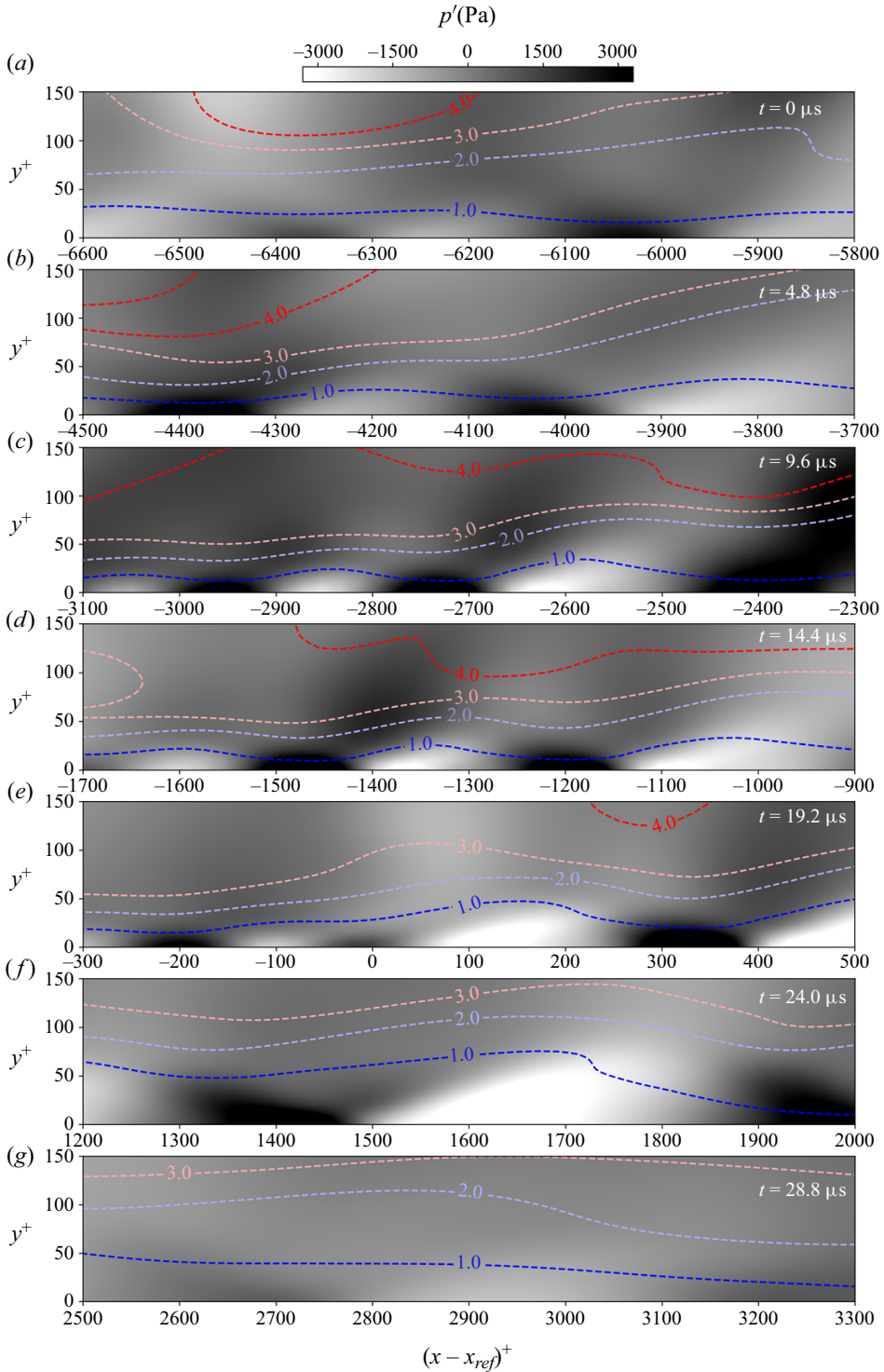


Figure 31. Contours of pressure fluctuations in the (x, y) plane below $y^+ = 150$ in M7.4-R4.1 at (a) $t = 0 \mu\text{s}$, (b) $t = 4.8 \mu\text{s}$, (c) $t = 9.6 \mu\text{s}$, (d) $t = 14.4 \mu\text{s}$, (e) $t = 19.2 \mu\text{s}$, (f) $t = 24.0 \mu\text{s}$ and (g) $t = 28.8 \mu\text{s}$. Contour lines of local Mach number are given by dashed lines. The visualized regions are selected along the white dash-dotted lines shown in figure 29.

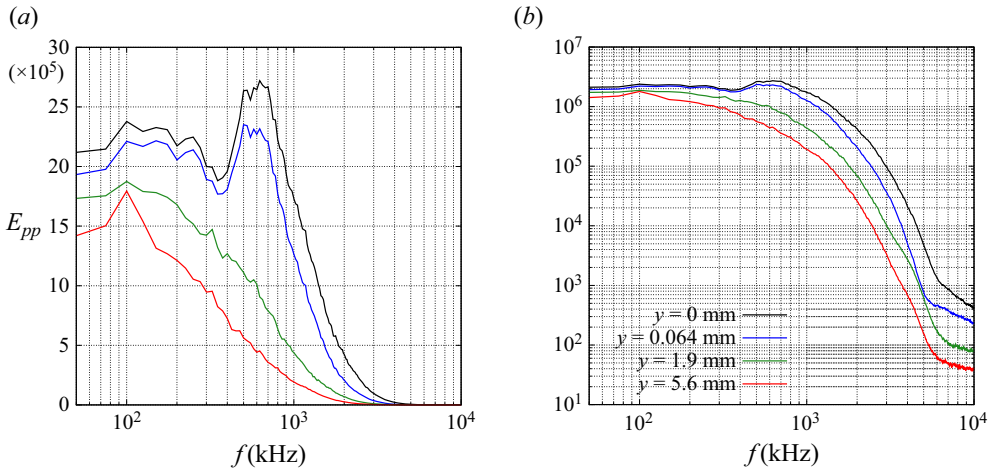


Figure 32. Energy spectra of pressure fluctuations in time at $x = 0.85$ m for the M7.4-R4.1 case for several y^* locations. The spectra are shown in (a) the linear scale and (b) the logarithmic scale.

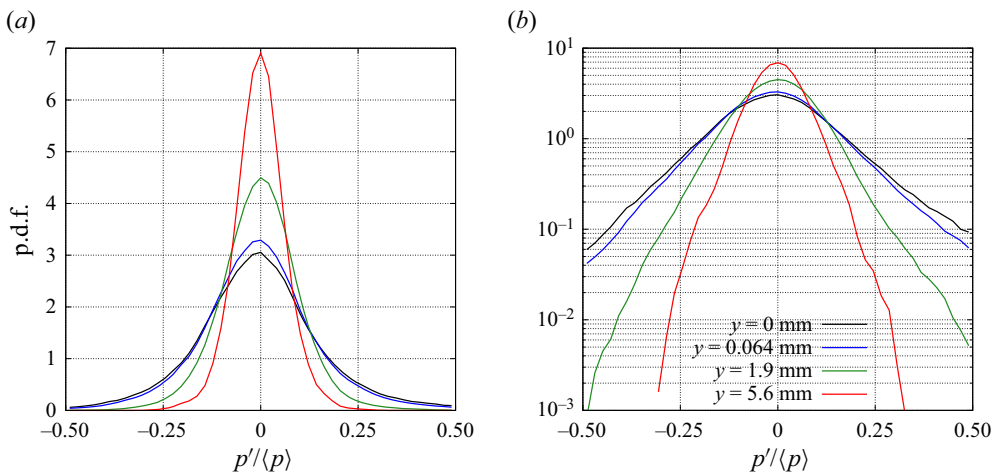


Figure 33. The p.d.f. of pressure fluctuations at $x = 0.85$ m for the M7.4-R4.1 case for several y^* locations. The data are shown in (a) the linear scale and (b) the logarithmic scale.

number are given by dashed lines. The wall unit y^+ is adopted because the semi-local unit y^* does not constitute a linear mapping against the wall-normal coordinates. From $t = 0$ to $t = 9.6 \mu\text{s}$, the wavelength becomes shorter and the fluctuation is enhanced only below $y^+ = 30$ ($y^* = 9$). Interestingly, these strong fluctuations extend to the contour line of Mach 1.0 and do not cross the line of Mach 2.0, indicating that the fluctuations are trapped by the sonic line as Chen & Scalo (2021b) expected; not to be confused with the relative sonic line, which is defined in the context of transitional hypersonic flows (Fedorov 2011). There is an uplift in the sonic line after $t = 14.4 \mu\text{s}$, reaching $y^+ = 50$ ($y^* = 15$) at $t = 24.0 \mu\text{s}$. The trapped waves remain attached to the wall until, in this particular example, they dissipate at $t = 28.8 \mu\text{s}$.

To quantitatively explore their behaviour, figure 32 provides energy spectra of pressure fluctuations in time at $x = 0.85$ m for several y locations and figure 33 shows the

probability density function (p.d.f.) of pressure fluctuations for the same locations. The sampling frequency is 25 MHz and the data are collected for 0.16 ms. The spectra are computed with the Hann window and segments of 1000 points and 70 % overlap.

The energy spectra at $y = 1.9$ mm and 5.6 mm show clear energy cascade from $f = 100$ to 5000 kHz. The sudden slope change around $f = 5000$ kHz corresponds to the frequency constraint due to the present grid resolution, as discussed in the authors' past work (Camillo *et al.* 2023). On the other hand, the spectra at the wall and $y = 0.064$ mm show a plateau peak between 500 and 700 kHz. The frequency is comparable to the estimated one of the trapped waves from figure 30, and thus this peak is attributed to the trapped waves. The absence of the peak for $y = 1.9$ mm and 5.6 mm is consistent with the non-existence of trapped waves over the sonic line in figure 31.

Figure 33 shows that the probability density at the wall and $y = 0.064$ mm extends from -0.5 to 0.5 , while the data for $y = 1.9$ and 5.6 mm are below 0.1 at $p'/\langle p \rangle = \pm 0.3$. As shown in figure 30, the trapped waves can be characterized by strong pressure fluctuations, and such strong fluctuations are not observed away from the wall. Therefore the p.d.f. for $|p'_w|/\langle p \rangle > 0.3$ mainly originates from the trapped waves. The probability of such strong pressure fluctuations can be obtained by integrating the p.d.f. at the wall for $|p'_w|/\langle p \rangle > 0.3$, and the integrated value is 7.3 %. This result indicates that strong pressure fluctuations associated with the trapped waves cover 7.3 % of the wall surface.

6. Conclusion

Large-eddy simulations of hypersonic boundary layers over a 7-degree half-angle cone has been performed to investigate the flow dynamics in highly cooled hypersonic turbulent boundary layers and explore the performance of the newly developed rescaling strategy: a volumetric rescaling method which extracts fluctuations from a series of streamwise locations and imposes rescaled fluctuations on a rescaling box that also extends in the streamwise direction. The Mach number is 7.4, and the Reynolds number per metre is $Re_m = 4.1 \times 10^6 \text{ m}^{-1}$ or $Re_m = 6.4 \times 10^6 \text{ m}^{-1}$. The wall temperature is 300 K, and the wall-to-recovery temperature ratio is around 0.1. The rescaling simulation with the lower Reynolds number was compared with the laminar-to-turbulent transition simulation under the same free-stream condition to examine the performance of the volumetric rescaling method. Furthermore, turbulent statistics and flow structures for the hypersonic boundary layers with the low wall-to-recovery temperature ratio were investigated.

The comparison with the laminar-to-turbulent transition simulation revealed that the volumetric rescaling simulation exhibits streaky structures of the streamwise velocity, which are quite similar to the laminar-to-turbulent transition one. The number of streaks in the azimuthal direction appears not to change with respect to the streamwise coordinates. The observation was supported by spectral analyses for the velocity and temperature fluctuations. Both of the spectra showed acceptable agreements downstream, indicating that the volumetric rescaling method can generate turbulent fluctuations with similar energy spectra to the laminar-to-turbulent transition simulation in the present conical geometry. Mean profiles and turbulent fluctuation correlations of velocity recover quickly, while the temperature variance in the volumetric rescaling simulation departs from the equilibrium state after the rescaling box and is the slowest among the variance profiles to relax to equilibrium. We hypothesize that the present rescaling strategy suffers from the inaccuracy of the mean temperature profiles of the precursor RANS calculation. However, fluctuations of temperature also recover the downstream, and the recovery length is around 43 times as long as the inlet boundary-layer thickness in the present Mach 7.4 case,

$Re_m = 4.1 \times 10^6 \text{ m}^{-1}$ or $Re_m = 6.4 \times 10^6 \text{ m}^{-1}$, and highly cooled condition ($T_w/T_r \sim 0.1$). The temperature–velocity relation in the rescaling box deviates from that in the laminar-to-turbulent transition simulation, whereas it collapses and achieves self-similarity downstream after the recovery process is completed, implying that the completion of the recovery process can be examined by the temperature–velocity relation.

The effects of the rescaling box size were examined by testing three different box sizes. Observation of pressure fluctuation fields revealed that unphysical fluctuation appears immediately after the rescaling box, and it induces numerical blow-up when the box size is too short. The unphysical fluctuation is reduced with the larger rescaling box, indicating that the volumetric rescaling strategy can stabilize the numerics for hypersonic inflows. On the other hand, a comparison of wall-heat flux and turbulent fluctuations clarified that the box size does not influence the downstream flow field as long as simulations are sustained. Thus, there should be an optimum length for the rescaling box.

Despite the present conical geometry, some existing correlations for the temperature–velocity relation originally developed for flat plate boundary layers show reasonable agreement with the rescaled LES flow fields. Velocity fluctuation correlations and turbulent Prandtl numbers qualitatively agree with the hypersonic boundary layers over flat plates. The present conical hypersonic boundary layers show an increase in pressure fluctuations in the vicinity of the wall, which are not observed in incompressible boundary layers. The near-wall-pressure fluctuations are correlated to density and temperature fluctuations around viscous sub-layers and the lower buffer layers. Velocity and temperature correlation exhibits strong similarity in the viscous sub-layers, whereas the correlation becomes anti-correlated over the buffer layer because of the sign switch in the temperature gradient. The SRA relation largely deviates from 1 in the entire boundary layer because of the total temperature variation due to the highly cooled wall. The HSRA of Huang *et al.* (1995) and its modified version by Zhang *et al.* (2014) were also investigated to account for the variation, however, they monotonically decrease toward the edge of the boundary layer and deviate from 1. Further modified relations calculated using Favre-averaged quantities can improve the analogy results, yielding similar magnitudes to previous investigations conducted on planar hypersonic boundary layers. A comparison between the two Reynolds-number cases shows good agreement in all investigated statistics, indicating that the general turbulent statistics are almost independent of the Reynolds number in the tested conditions.

Flow fields in the vicinity of the wall show streaky structures, which have quite thin spacing in the azimuthal direction and long ones in the streamwise direction due to the low wall-to-recovery temperature ratio. The velocity and temperature fields exhibit similar structures, which are consistent with the temperature–velocity correlation coefficient near the wall. The temperature field has highly localized fluctuations in low-temperature streaks. Since the density field reflects the temperature one, it shows similar patterns in high-density streaks. On the other hand, such fluctuations are not observable in the inner layer or outer layer, indicating that the localized fluctuations are associated with the near-wall phenomena. The similarity between the velocity and temperature becomes weaker on going away from the wall as well as for supersonic or subsonic compressible boundary layers.

Visualization of pressure fluctuations at the wall revealed that strong pressure oscillations are similar to second-mode waves in cooled hypersonic laminar boundary layers. Such phenomena were also observed in supersonic and hypersonic channel flows, and they are called trapped waves. The fluid temperature locally becomes below the wall temperature near the wall because strong fluid expansion is locally induced by the trapped

wave. As a result, wall-heat flux shows local negative values, indicating that the boundary layer locally absorbs heat from the wall against the statistical direction. Observation of a time series of the pressure fluctuation field revealed that the wavelength of the trapped waves is approximately 0.17 to 0.5 times as long as the boundary-layer thickness and they propagate at Mach 4.5 based on the wall temperature. In addition, the trapped waves repeatedly appear and disappear and do not circulate in the rescaling domain. Visualization in the streamwise wall-normal plane revealed that the waves are trapped by the sonic line similarly to the second mode wave and remain attached to the wall. The occurrence of the trapped waves indicates that the second-mode instability in the hypersonic regime is important even in turbulent boundary layers. Spectral analysis for the pressure fluctuations clarified that the trapped wave frequency is between 500 and 700 kHz. The analyses based on the probability density function clarified that strong pressure fluctuations associated with the trapped waves cover 7.3 % of the wall surface.

Acknowledgements. The authors acknowledge the computational support of the Rosen Center for Advanced Computing (RCAC) at Purdue.

Funding. The authors acknowledge support through ONR grant no. N00014-20-1-2662 (ONR-YIP, PI: C.S.), N00014-21-1-2475 (ONR-MURI, PI: Venkat Raman), and N00014-23-1-2560 (Core ONR program, PI: C.S.) with Dr E. Marineau as Program Manager. This work used Purdue Anvil CPU at Purdue through allocation MCH220038 from the Advanced Cyberinfrastructure Coordination Ecosystem: Services & Support (ACCESS) program, which is supported by National Science Foundation grant nos 2138259, 2138286, 2138307, 2137603 and 2138296 (Boerner *et al.* 2023).

Declaration of interests. The authors report no conflict of interest.

Author ORCIDs.

-  Takahiko Toki <https://orcid.org/0000-0002-3408-0681>;
-  Victor C.B. Sousa <https://orcid.org/0000-0001-6406-7595>;
-  Yongkai Chen <https://orcid.org/0000-0002-5243-8341>;
-  Giannino Ponchio Camillo <https://orcid.org/0000-0002-2178-0777>;
-  Alexander Wagner <https://orcid.org/0000-0002-9700-1522>;
-  Carlo Scalo <https://orcid.org/0000-0002-6774-2207>.

Appendix A. Distance between rescaling and recycling boxes

The distance between the rescaling and recycling boxes needs to be sufficiently large because the rescaling method is a pseudo-periodic condition. The distance is generally confirmed by two-point correlations in the same manner as periodic flows. Figure 34 shows two-point correlations of streamwise velocity, temperature and density components for the centre of the rescaling box in the streamwise direction. The correlations are computed for the $y^* = 10$ plane of M7.4-R4.1 and M7.4-R6.4. The strong correlations are observable at the centre of the recycling box since fluctuations at this location are recycled and imposed in the rescaling box. Decorrelation of all components is achieved for $0.65 \text{ m} < x < 0.8 \text{ m}$, indicating that the distance is sufficiently long. Theoretically, the recycling box can be located closer to the rescaling box as far as the decorrelation holds. However, the closer distance may result in the introduction of spurious frequencies/periodic flow structures in the computational domain, and thus the present recycling box is located at the furthest downstream location.

The required distance is expected to depend on flow conditions. Since Mach number and wall-to-recovery temperature ratios elongate velocity streaks (Coleman *et al.* 1995; Duan *et al.* 2010), it is likely that a longer length is required for the decorrelation as Mach number increases or wall temperature decreases. On the other hand, databases for such conditions

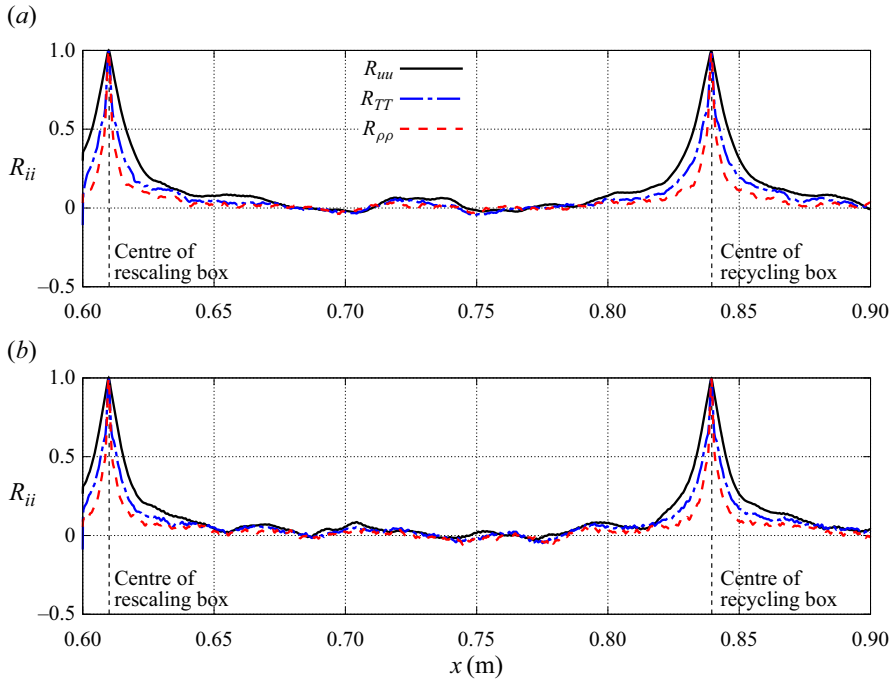


Figure 34. Two-point correlations of streamwise velocity, temperature and density components for the centre of the rescaling box in the streamwise direction. The data are obtained at $y^* = 10$ for (a) M7.4-R4.1 and (b) M7.4-R6.4.

Case	Length of outlet sponge	Length of upper sponge
Adopted sponge	$0.03L_x$	$0.05L_y$
Shorter outlet sponge	$0.02L_x$	$0.05L_y$
Longer outlet sponge	$0.06L_x$	$0.05L_y$
Shorter upper sponge	$0.03L_x$	$0.025L_y$
Longer upper sponge	$0.03L_x$	$0.075L_y$

Table 5. List of the tested sponge conditions.

are relatively limited, and it is difficult to quantitatively expect the decorrelation length by *a priori* study. Therefore the required distance between the rescaling and recycling regions needs to be examined *a posteriori*.

Appendix B. Effects of sponge boundaries

The present study adopts sponge boundaries at the upper and outlet boundaries. To investigate the effects of the sponge boundaries on turbulent statistics, multiple sponge lengths are tested for M7.4-R4.1 as summarized in table 5. A coarse mesh of $N_x \times N_y \times N_\theta = 960 \times 128 \times 84$ is used in these tests. Figure 35 compares fluctuation correlations of streamwise velocity and temperature at $x = 0.85$ m among the cases. The data show excellent collapses, indicating that turbulent correlations at this location are insensitive to the length of sponge layers. Thus, the current sponge boundaries do not contaminate turbulent correlations and the development of the boundary layer.

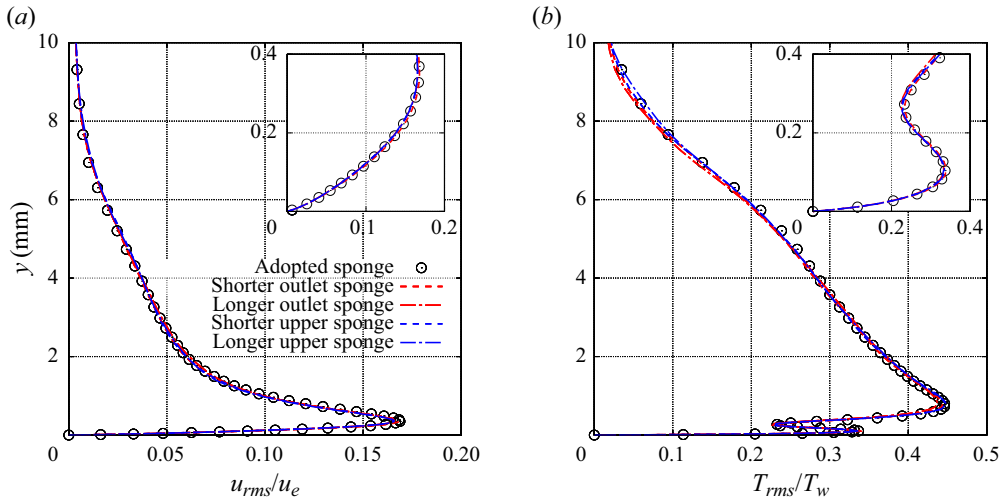


Figure 35. Effects of sponge boundary conditions on fluctuation correlations at $x = 0.85$ m for (a) streamwise velocity and (b) temperature.

REFERENCES

AIKEN, T.T., BOYD, I.D., DUAN, L. & HUANG, J. 2022 Assessment of Reynolds averaged Navier–Stokes models for a hypersonic cold-wall turbulent boundary layer. *AIAA Paper 2022-0586*. AIAA SciTech 2022 Forum.

ALBA, C., CASPER, K., BERESH, S. & SCHNEIDER, S. 2010 Comparison of experimentally measured and computed second-mode disturbances in hypersonic boundary-layers. In *48th AIAA Aerospace Sciences Meeting Including the New Horizons Forum and Aerospace Exposition*. *AIAA Paper 2010-897*. American Institute of Aeronautics and Astronautics.

ARAYA, G., CASTILLO, L., MENEVEAU, C. & JANSEN, K. 2011 A dynamic multi-scale approach for turbulent inflow boundary conditions in spatially developing flows. *J. Fluid Mech.* **670**, 581–605.

BAI, T., GRIFFIN, K.P. & FU, L. 2022 Compressible velocity transformations for various noncanonical wall-bounded turbulent flows. *AIAA J.* **60**, 4325–4337.

BERTIN, J.J. & CUMMINGS, R.M. 2006 Critical hypersonic aerothermodynamic phenomena. *Annu. Rev. Fluid Mech.* **38**, 129–157.

BOERNER, T.J., DEEMS, S., FURLANI, T.R., KNUTH, S.L. & TOWNS, J. 2023 ACCESS: advancing innovation: NSF’s advanced cyberinfrastructure coordination ecosystem: services & support. In *Practice and Experience in Advanced Research Computing (PEARC’23)*. Association for Computing Machinery.

BRADSHAW, P. 1977 Compressible turbulent shear layers. *Annu. Rev. Fluid Mech.* **9**, 33–54.

BUSEMANN, A. 1931 *Handbuch der Experimentalphysik*, vol. 4. Geest und Port.

CAMILLO, G.P., WAGNER, A., TOKI, T. & SCALO, C. 2023 Combined experimental and numerical investigation of a hypersonic turbulent boundary layer by means of FLDI and large-eddy simulations. *Aerospace* **10**, 570.

CARY, A.W., CHAWNER, J., DUQUE, E.P., GROPP, W., KLEB, W.L., KOLONAY, R.M., NIELSEN, E. & SMITH, B. 2021 CFD vision 2030 road map: progress and perspectives. AIAA Aviation 2021 Forum.

CASPER, K., BERESH, S., HENFLING, J., SPILLERS, R., PRUETT, B. & SCHNEIDER, S. 2009 Hypersonic wind-tunnel measurements of boundary-layer pressure fluctuations. In *39th AIAA Fluid Dynamics Conference*. *AIAA Paper 2009-4054*. American Institute of Aeronautics and Astronautics.

CASPER, K.M., BERESH, S.J., HENFLING, J.F., SPILLERS, R.W., PRUETT, B.O.M. & SCHNEIDER, S.P. 2016 Hypersonic wind-tunnel measurements of boundary-layer transition on a slender cone. *AIAA J.* **54** (4), 1250–1263.

CASPER, K.M., BERESH, S.J., WAGNILD, R.M., HENFLING, J.F., SPILLERS, R.W. & PRUETT, B.O.M. 2013 Simultaneous pressure measurements and high-speedschlieren imaging of disturbances in a transitionhypersonic boundary layer. In *43rd Fluid Dynamics Conference*. *AIAA Paper 2013-2739*. American Institute of Aeronautics and Astronautics.

- CECI, A., PALUMBO, A., LARSSON, J. & PIROZZOLI, S. 2022 Numerical tripping of high-speed turbulent boundary layers. *Theor. Comput. Fluid Dyn.* **36**, 865–886.
- CHAPELIER, J.-B. & LODATO, G. 2016 A spectral-element dynamic model for the large-eddy simulation of turbulent flows. *J. Comput. Phys.* **321**, 279–302.
- CHEN, X., GAN, J. & FU, L. 2024 An improved Baldwin–Lomax algebraic wall model for high-speed canonical turbulent boundary layers using established scalings. *J. Fluid Mech.* **987**, A7.
- CHEN, Y. & SCALO, C. 2021a Effects of porous walls on near-wall supersonic turbulence. *Phys. Rev. Fluids* **6**, 084607.
- CHEN, Y. & SCALO, C. 2021b Trapped waves in supersonic and hypersonic turbulent channel flow over porous walls. *J. Fluid Mech.* **920**, A24.
- COLEMAN, G.N., KIM, J. & MOSER, R.D. 1995 A numerical study of turbulent supersonic isothermal-wall channel flow. *J. Fluid Mech.* **305**, 159–183.
- CROCCO, L. 1932 Sulla trasmissione del calore da una lamina piana a un fluido scorrente ad alta velocita. *L'Aerotecnica* **12**, 181–197.
- DANIS, M.E. & DURBIN, P. 2022 Compressibility correction to k - ω models for hypersonic turbulent boundary layers. *AIAA J.* **60** (11), 6225–6234.
- DEUTSCHES ZENTRUM FÜR LUFT - UND RAUMFAHRT (DLR) 2018 The high enthalpy shock tunnel Göttingen of the German Aerospace Center (DLR). *J. Large-Scale Res. Facilities* **4**, A133.
- DHAMANKARA, N.S., BLAISDELLA, G.A. & LYRINTZISB, A.S. 2016 A simple extension of digital filter-based turbulent inflow to non-uniform structured grids. *Aerosp. Sci. Technol.* **56**, 29–33.
- DI RENZO, M. & URZAY, J. 2021 Direct numerical simulation of a hypersonic transitional boundary layer at suborbital enthalpies. *J. Fluid Mech.* **912**, A29.
- DORRANCE, W.H. 1962 *Viscous Hypersonic Flow*. McGraw-Hill.
- VAN DRIEST, E.R. 1951 Turbulent boundary layer in compressible fluids. *J. Aeronaut. Sci.* **18**, 145–160.
- DUAN, L., BEEKMAN, I. & MARTIN, M.P. 2010 Direct numerical simulation of hypersonic turbulent boundary layers. Part 2. Effect of wall temperature. *J. Fluid Mech.* **655**, 419–445.
- DUAN, L., BEEKMAN, I. & MARTIN, M.P. 2011 Direct numerical simulation of hypersonic turbulent boundary layers. Part 3. Effect of Mach number. *J. Fluid Mech.* **672**, 245–267.
- DUAN, L., CHOUDHARI, M.M. & WU, M. 2014 Numerical study of acoustic radiation due to a supersonic turbulent boundary layer. *J. Fluid Mech.* **746**, 165–192.
- DUAN, L., CHOUDHARI, M.M. & ZHANG, C. 2016 Pressure fluctuations induced by a hypersonic turbulent boundary layer. *J. Fluid Mech.* **804**, 578–607.
- DUAN, L. & MARTIN, M.P. 2011 Direct numerical simulation of hypersonic turbulent boundary layers. Part 4. Effect of high enthalpy. *J. Fluid Mech.* **684**, 25–59.
- FEDOROV, A. 2011 Transition and stability of high-speed boundary layers. *Annu. Rev. Fluid Mech.* **43**, 79–95.
- FERNHOLZ, H.H. & FINLEY, P.J. 1980 A critical commentary on mean flow data for two-dimensional compressible turbulent boundary layers. AGARD-AG-253.
- FRISCH, U. 1995 *Turbulence: The Legacy of A. N. Kolmogorov*. Cambridge University Press.
- GAVIGLIO, J. 1987 Reynolds analogies and experimental study of heat transfer in the supersonic boundary layer. *Int'l J. Heat Mass Transfer* **30** (5), 911–926.
- GOTTLIEB, S. 2005 On high order strong stability preserving Runge-Kutta and multi step time discretizations. *J. Sci. Comput.* **25**, 105–128.
- GRIFFIN, K.P., FU, L. & MOIN, P. 2021 Velocity transformation for compressible wall-bounded turbulent flows with and without heat transfer. *Proc. Natl Acad. Sci. USA* **118** (34), e2111144118.
- GRIFFIN, K.P., FU, L. & MOIN, P. 2023 Near-wall model for compressible turbulent boundary layers based on an inverse velocity transformation. *J. Fluid Mech.* **970**, A36.
- GUPTA, P. & SCALO, C. 2018 Spectral energy cascade and decay in nonlinear acoustic waves. *Phys. Rev. E* **98**, 033117.
- HASAN, A.M., LARSSON, J., PIROZZOLI, S. & PECNIK, R. 2023 Incorporating intrinsic compressibility effects in velocity transformations for wall-bounded turbulent flows. *Phys. Rev. Fluids* **8**, L112601.
- HENDRICKSON, T., SUBBAREDDY, P.K. & CANDLER, G.V. 2022 Improving eddy viscosity based turbulence models for high speed, cold wall flows. *AIAA Paper 2022-0589*. AIAA Scitech 2022 Forum.
- HENDRICKSON, T., SUBBAREDDY, P.K., CANDLER, G.V. & MACDONALD, R.L. 2023 Applying compressible transformations to wall modeled les of cold wall flat plate boundary layers. *AIAA Paper 2023-2635*. AIAA Scitech 2023 Forum.
- HUANG, J., DUAN, L., CASPER, K.M., WAGNILD, R.M. & BITTER, N.P. 2024 Transducer resolution effect on pressure fluctuations beneath hypersonic turbulent boundary layers. *AIAA J.* **62**, 882–895.
- HUANG, J., DUAN, L. & CHOUDHARI, M.M. 2022 Direct numerical simulation of hypersonic turbulent boundary layers: effect of spatial evolution and Reynolds number. *J. Fluid Mech.* **937**, A3.

- HUANG, J., NICHOLSON, G.L., DUAN, L., CHOUDHARI, M.M. & BOWERSOX, R.D.W. 2020 Simulation and modeling of cold-wall hypersonic turbulent boundary layers on flat plate. *AIAA Paper* 2020-0571. AIAA SciTech 2020 Forum.
- HUANG, P.G., BRADSHAW, P. & COAKLEY, T.J. 1993 Skin friction and velocity profile family for compressible turbulent boundary layers. *AIAA J.* **31** (9), 1600–1604.
- HUANG, P.G., COLEMAN, G.N. & BRADSHAW, P. 1995 Compressible turbulent channel flows: DNS results and modelling. *J. Fluid Mech.* **305**, 185–218.
- JORDAN, S.A. 1999 A large-eddy simulation methodology in generalized curvilinear coordinates. *J. Comput. Phys.* **148** (2), 322–340.
- KAWAI, S. 2019 Heated transcritical and unheated non-transcritical turbulent boundary layers at supercritical pressures. *J. Fluid Mech.* **865**, 563–601.
- KIANVASHRAD, N. & KNIGHT, D. 2021 Large eddy simulation of hypersonic turbulent boundary layers. *Fluids* **6**, 449.
- LAGHA, M., KIM, J., ELDRIDGE, J.D. & ZHONG, X. 2011 A numerical study of compressible turbulent boundary layers. *Phys. Fluids* **23** (1), 015106.
- LEES, L. 1956 Laminar heat transfer over blunt-nosed bodies at hypersonic flight speeds. *J. Jet Propul.* **26** (4), 259–269.
- LELE, S.K. 1992 Compact finite difference schemes with spectral-like resolution. *J. Comput. Phys.* **103** (1), 16–42.
- LI, Q., SCHLATTER, P., BRANDT, L. & HENNINGSON, D.S. 2009 DNS of a spatially developing turbulent boundary layer with passive scalar transport. *Intl J. Heat Fluid Flow* **30**, 916–929.
- LI, X., FU, D. & MA, Y. 2008 Direct numerical simulation of hypersonic boundary-layer transition over a blunt cone. *AIAA J.* **46** (11), 2899–2913.
- LUND, T.S., WU, X. & SQUIRES, K.D. 1998 Generation of turbulent inflow data for spatially-developing boundary layer simulations. *J. Comput. Phys.* **140**, 233–258.
- MARTIN, M.P. 2004 DNS of hypersonic turbulent boundary layers. In *34th AIAA Fluid Dynamics Conference and Exhibit*. AIAA Paper 2004-2337. American Institute of Aeronautics and Astronautics.
- MARTIN, M.P. 2007 Direct numerical simulation of hypersonic turbulent boundary layers. Part 1. Initialization and comparison with experiments. *J. Fluid Mech.* **570**, 347–364.
- MCDANIEL, D.R., NICHOLS, R.H., EYMANN, T.A., STARR, R.E. & MORTON, S.A. 2016 Accuracy and performance improvements to Kestrel’s near-body flow solver. *AIAA Paper* 2016-1051. AIAA Aviation 2021 Forum.
- MORGAN, B., LARSSON, J., KAWAI, S. & LELE, S.K. 2011 Improving low-frequency characteristics of recycling/rescaling inflow turbulence generation. *AIAA J.* **49** (3), 582–597.
- MORKOVIN, M.V. 1962 Effects of compressibility on turbulent flows. *Méc. Turbul.* **367**, 380.
- NAGARAJAN, S., LELE, S.K. & FERZIGER, J.H. 2003 A robust high-order compact method for large eddy simulation. *J. Comput. Phys.* **191**, 392–419.
- NAGARAJAN, S., LELE, S.K. & FERZIGER, J.H. 2007 Leading-edge effects in bypass transition. *J. Fluid Mech.* **572**, 471–504.
- NICHOLS, R.H. 2019 A summary of the turbulence models in the CREATETM-AV Kestrel flow solvers. *AIAA Paper* 2019-1342. AIAA Scitech 2019 Forum.
- PARISH, E., CHING, D.S., MILLER, N.E., BERESH, S.J. & BARONE, M.F. 2023 Turbulence modeling for compressible flows using discrepancy tensor-basis neural networks and extrapolation detection. *AIAA Paper* 2023-2126. AIAA SciTech 2023 Forum.
- PASSIATORE, D., SCIACOVELLI, L., CINNELLA, P. & PASCAZIO, G. 2021 Finite-rate chemistry effects in turbulent hypersonic boundary layers: a direct numerical simulation study. *Phys. Rev. Fluids* **6**, 054604.
- PASSIATORE, D., SCIACOVELLI, L., CINNELLA, P. & PASCAZIO, G. 2022 Thermochemical non-equilibrium effects in turbulent hypersonic boundary layers. *J. Fluid Mech.* **941**, A21.
- PATI, B., TOKI, T., SINGH, R., AHMED, S., DUAN, L. & SCALO, C. 2024 Comparison of direct-numerical and large-eddy simulations of Mach 11 hypersonic turbulent flow over a flat plate. *AIAA Paper* 2024-3910. AIAA Aviation 2024 Forum.
- PIOMELLI, U., ROUHI, A. & GEURTS, B.J. 2015 A grid-independent length scale for large-eddy simulations. *J. Fluid Mech.* **766**, 499–527.
- PIROZZOLI, S. & BERNARDINI, M. 2011 Turbulence in supersonic boundary layers at moderate Reynolds numbers. *J. Fluid Mech.* **688**, 120–168.
- ROY, D., KUCHTA, B. & DUAN, L. 2024 Surface shear-stress and wall heat-flux fluctuations induced by a hypersonic turbulent boundary layer. *AIAA Paper* 2024-0885. AIAA Scitech 2024 Forum.
- RUBESIN, M.W. 1990 Extra compressibility terms for favre-averaged two-equation models of inhomogeneous turbulent flows. *NASA Tech. Rep.* CR-177556.

- RUMSEY, C.L. 2010 Compressibility considerations for k - ω turbulence models in hypersonic boundary-layer applications. *J. Spacecr. Rockets* **47** (1), 11–20.
- SAGAUT, P., GARNIER, E., TROMEUR, E., LARCHEVÈQUE, L. & LABOURASSE, E. 2004 Turbulent inflow conditions for large-eddy simulation of compressible wall-bounded flows. *AIAA J.* **42** (3), 469–477.
- SCHLATTER, P. & ÖRLÜ, R. 2010 Assessment of direct numerical simulation data of turbulent boundary layers. *J. Fluid Mech.* **659**, 116–126.
- SHADLOO, M.S., HADJADJ, A. & HUSSAIN, F. 2015 Statistical behavior of supersonic turbulent boundary layers with heat transfer at $M_\infty = 2$. *Intl J. Heat Fluid Flow* **53**, 113–134.
- SIMENS, M.P., JIMÉNEZ, J., HOYAS, S. & MIZUNO, Y. 2009 A high-resolution code for turbulent boundary layers. *J. Comput. Phys.* **228**, 4218–4231.
- SIVASUBRAMANIAN, J. & FASEL, H.F. 2015 Direct numerical simulation of transition in a sharp cone boundary layer at Mach 6: fundamental breakdown. *J. Fluid Mech.* **768**, 175–218.
- SLOTNICK, J., KHODADOUST, A., ALONSO, J., DARMOFAL, D., GROPP, W., LURIE, E. & MAVRIPLIS, D. 2014 CFD vision 2030 study: a path to revolutionary computational aerosciences. *NASA Tech. Rep.* NASA/CR-2014-218178.
- SOUSA, V.C.B., PATEL, D., CHAPELIER, J.-B., WARTEMANN, V., WAGNER, A. & SCALO, C. 2019 Numerical investigation of second-mode attenuation over carbon/carbon porous surfaces. *J. Spacecr. Rockets* **56** (2), 319–332.
- SOUSA, V.C.B. & SCALO, C. 2022a A legendre spectral viscosity (LSV) method applied to shock capturing for high-order flux reconstruction schemes. *J. Comput. Phys.* **460**, 111157.
- SOUSA, V.C.B. & SCALO, C. 2022b A unified quasi-spectral viscosity (QSV) approach to shock capturing and large-eddy simulation. *J. Comput. Phys.* **459**, 111139.
- SOUSA, V.C.B., WARTEMANN, V., WAGNER, A. & SCALO, C. 2023 Linear stability analysis of second-mode attenuation via porous carbon-matrix ceramics. *Phys. Fluids* **35**, 064113.
- SOUSA, V.C.B., WARTEMANN, V., WAGNER, A. & SCALO, C. 2024 Dynamic large-eddy simulation of hypersonic transition delay over broadband wall impedance. *J. Fluid Mech.* **999**, A41.
- SPALART, P.R. & ALLMARAS, S.R. 1992 A one-equation turbulence model for aerodynamic flow. In *30th Aerospace Sciences Meeting and Exhibit*. AIAA-92-0439. American Institute of Aeronautics and Astronautics.
- STOLZ, S. & ADAMS, N.A. 2003 Large-eddy simulation of high-Reynolds-number supersonic boundary layers using the approximate deconvolution model and a rescaling and recycling technique. *Phys. Fluids* **15** (8), 2398–2412.
- TANG, J., ZHAO, Z., WAN, Z.-H. & LIU, N.-S. 2020 On the near-wall structures and statistics of fluctuating pressure in compressible turbulent channel flows. *Phys. Fluids* **32**, 115121.
- TAYLOR, G.I. & MACCOLL, J.W. 1933 The air pressure on a cone moving at high speeds-I. *Proc. R. Soc. Lond. Ser. A* **139**, 278–297.
- TOKI, T. & BELLAN, J. 2021 Investigation of species-mass diffusion in binary-species boundary layers at high pressure using direct numerical simulations. *J. Fluid Mech.* **928**, A18.
- TOKI, T. & BELLAN, J. 2022 Effects of thermophoresis on high pressure binary-species boundary layers with uniform and non-uniform compositions. *J. Fluid Mech.* **952**, A37.
- TOKI, T., SOUSA, V.C.B., CHEN, Y. & SCALO, C. 2024 Sub-filter-scale shear stress analysis in hypersonic turbulent Couette flow. *J. Fluid Mech.* **984**, A53.
- TOKI, T., TERAMOTO, S. & OKAMOTO, K. 2020 Velocity and temperature profiles in turbulent channel flow at supercritical pressure. *J. Propul. Power* **36**, 3–13.
- TRETTEL, A. & LARSSON, J. 2016 Mean velocity scaling for compressible wall turbulence with heat transfer. *Phys. Fluids* **28**, 026102.
- URBIN, G. & KNIGHT, D. 2001 Large-eddy simulation of a supersonic boundary layer using an unstructured grid. *AIAA J.* **39** (7), 1288–1295.
- VOLPIANI, P.S., IYER, P.S., PIROZZOLI, S. & LARSSON, J. 2020 Data-driven compressibility transformation for turbulent wall layers. *Phys. Rev. Fluids* **5**, 052602(R).
- WAGNER, A. 2014 Passive hypersonic boundary layer transition control using ultrasonically absorptive carbon-carbon ceramic with random microstructure. PhD thesis, Katholieke Universiteit, Leuven.
- WAGNER, A., KUHN, M., SCHRAMM, J.M. & HANNEMANN, K. 2013 Experiments on passive hypersonic boundary layer control using ultrasonically absorptive carbon-carbon material with random microstructure. *Exp. Fluids* **54** (10), 1606.
- WAGNER, A., WARTEMANN, V., DITTERT, C. & KÜTEMAYER, M. 2019 Passive hypersonic transition control by means of ultrasonically absorptive thermal protection materials (UAT). *Tech. Rep.* AFRL-AFOSR-UK-TR-2020-0025. DTIC.

LES of conical hypersonic boundary layers

- WALZ, A. 1959 Compressible turbulent boundary layers with heat transfer and pressure gradient in flow direction. *J. Res. Natl Bur. Stand. B Math. Math. Phys.* **63B**, 53–72.
- WHITE, F.M. 2006 *Viscous Fluid Flow*, 3rd edn. McGraw-Hill.
- WILCOX, D.C. 2006 *Turbulence Modeling for CFD*, 3rd edn. DCW Industries.
- XU, D., WANG, J. & CHEN, S. 2022 Skin-friction and heat-transfer decompositions in hypersonic transitional and turbulent boundary layers. *J. Fluid Mech.* **941**, A4.
- XU, D., WANG, J. & CHEN, S. 2023 Reynolds number and wall cooling effects on correlations between the thermodynamic variables in hypersonic turbulent boundary layers. *J. Fluid Mech.* **965**, A4.
- XU, D., WANG, J., WAN, M., YU, C., LI, X. & CHEN, S. 2021a Compressibility effect in hypersonic boundary layer with isothermal wall condition. *Phys. Rev. Fluids* **6**, 054609.
- XU, D., WANG, J., WAN, M., YU, C., LI, X. & CHEN, S. 2021b Effect of wall temperature on the kinetic energy transfer in a hypersonic turbulent boundary layer. *J. Fluid Mech.* **929**, A33.
- XU, S. & MARTIN, M.P. 2004 Assessment of inflow boundary conditions for compressible turbulent boundary layers. *Phys. Fluids* **16** (7), 2623–2639.
- XUE, Y., FENG, Y. & ZHENG, X. 2024 Assessment of compressibility corrections on Spalart–Allmaras turbulence model for high-Mach-number flows. *AIAA J.* **62**, 92–107.
- ZHANG, C., DUAN, L. & CHOUDHARI, M.M. 2018 Direct numerical simulation database for supersonic and hypersonic turbulent boundary layers. *AIAA J.* **56** (11), 4297–4311.
- ZHANG, Y.-S., BI, W.-T., HUSSAIN, F., LI, X.-L. & SHE, Z.-S. 2012 Mach-number-invariant mean-velocity profile of compressible turbulent boundary layers. *Phys. Rev. Lett.* **109**, 054502.
- ZHANG, Y.-S., BI, W.-T., HUSSAIN, F. & SHE, Z.-S. 2014 A generalized Reynolds analogy for compressible wall-bounded turbulent flows. *J. Fluid Mech.* **739**, 392–420.